



저작자표시-비영리-변경금지 2.0 대한민국

이용자는 아래의 조건을 따르는 경우에 한하여 자유롭게

- 이 저작물을 복제, 배포, 전송, 전시, 공연 및 방송할 수 있습니다.

다음과 같은 조건을 따라야 합니다:



저작자표시. 귀하는 원저작자를 표시하여야 합니다.



비영리. 귀하는 이 저작물을 영리 목적으로 이용할 수 없습니다.



변경금지. 귀하는 이 저작물을 개작, 변형 또는 가공할 수 없습니다.

- 귀하는, 이 저작물의 재이용이나 배포의 경우, 이 저작물에 적용된 이용허락조건을 명확하게 나타내어야 합니다.
- 저작권자로부터 별도의 허가를 받으면 이러한 조건들은 적용되지 않습니다.

저작권법에 따른 이용자의 권리는 위의 내용에 의하여 영향을 받지 않습니다.

이것은 [이용허락규약\(Legal Code\)](#)을 이해하기 쉽게 요약한 것입니다.

[Disclaimer](#)

공학석사학위논문

**Pogo Instability Analysis of a
Clustered Liquid Rocket with
Sophisticated Branch Feedline**

복잡 관망을 포함한 클러스터 액체 추진 로켓의
포고 불안정성 해석

2021년 2월

서울대학교 대학원
협동과정 우주시스템 전공
유 정 욱

Abstract

Pogo Instability Analysis of a Clustered Liquid Rocket with Sophisticated Branch Feedline

JeongUk Yoo

Interdisciplinary Program in Space System

The Graduate School

Seoul National University

Pogo phenomenon is an instability that occurs in a liquid propellant space launch vehicle. When the increased frequencies of the fuselage modes along with fuel consumption coincide with those of the feedline pressure perturbations, longitudinal instability may occur. In this thesis, pogo analysis is carried out using the numerical results obtained from analysis of the fuselage structure, oxidizer feedline, and the propulsion system. By reinforcing the existing numerical analysis of the fuselage and the feedline system, brand new closed loop control system is constructed.

For the fuselage analysis, the structural response of Atlas-Surveyor fuselage is analyzed in high fidelity. Accurate transfer functions are acquired, which are then compared with those obtained by the existing lumped parameter methodology. Also, a clustered liquid propellant engine rocket is analyzed

considering the branch pipe in detail. LOX transmission line is modeled in a two-way branch configuration to account for the effect of the dual clustered engine. The transfer function of the propulsion system including a turbo-pump and a combustion chamber is aligned in parallel, with each set joining the exit of the corresponding branch-pipe. Thrust perturbation produced by each engine is fed back to an input of the fuselage transfer function respectively. This will enable the feedback oscillations to be either cancelled or overlapped depending on the phase difference, causing undesirable frequency response. To obtain reliable results for the fluid transmission line modeling, inducer-caused cavitation effect is also included by the rule of mixtures. The current results reveal that the flow distribution of LOX propellant through the branched feedline model suppresses the pressure fluctuation, thus improving the stability.

Simulation-based pogo phenomenon is constructed with careful observation of the combined launch vehicle fuselage-feedline transfer function. With accurate reconstruction of pogo resonance, change in the resonance is observed quantitatively.

Keywords: Space launch vehicle, Pogo instability, Pogo accumulator, Longitudinal mode analysis, Clustered rocket, Branched feedline

Student Number : 2019-21768

Contents

	Page
Abstract	i
Contents	iii
List of Tables	v
List of Figures	vi
List of Symbols	viii
Preface	x
Chapter 1 Introduction	1
1.1 Background.....	1
1.2 Previous Examinations	5
1.2.1 Fuselage Analysis.....	5
1.2.2 Feedline Analysis.....	5
Chapter 2 Pogo Analysis Formulation	7
2.1 Fuselage-Feedline Dynamic System.....	9
2.2 Fuselage Transfer Function $G(s)$	13
2.3 Feedline Transfer Function $H(s)$	19
2.4 Combined Transfer Function	28
Chapter 3 Verification and Application	30
3.1 Verification of the Fuselage Response.....	30
3.2 Verification of the Feedline Acoustic Mode	44
Chapter 4 Pogo Instability Analysis	56

Chapter 5 Conclusion and Future Works	60
5.1 Conclusion.....	60
5.2 Future Works.....	62
Acknowledgments	63
References	64
국문초록	69

List of Tables

	Page
Table 1 Types of the damping matrix and application.....	26
Table 2 Types of the fuselage modes.....	31
Table 3 Rearrangement of the longitudinal mode by the modal participation factor	31
Table 4 Comparison of the resonant frequencies by lumped parameter methodology and high fidelity representation.....	36
Table 5 Comparison of the dominant modes regarding the fuel balance dependency.....	38
Table 6 Fuselage mode comparison between the single and branch passage feedline.....	43
Table 7 Feedline mode frequencies against the experimental results.....	46
Table 8 Operating condition and the material properties of the feedline	48
Table 9 Geometric properties and operating conditions for the single and branch passage feedlines	54

List of Figures

	Page
Fig. 1.1 Various configurations of LOX feedline	3
Fig. 1.2 Clustered rocket system of KSLV-II [9].....	4
Fig. 2.1 Numerical integration procedure for a clustered engine rocket	8
Fig. 2.2 Integrated procedure for pogo analysis for a liquid propulsion rocket.....	10
Fig. 2.3 Finite element model based on Atlas launch vehicle	14
Fig. 2.4 Constant pressure/volume heat capacity for the present operating pressure and temperature.....	21
Fig. 2.5 Fluid transmission line of a branched LOX feedline	24
Fig. 3.1 Difference for the longitudinal modal displacement between the lumped and high-fidelity representation.....	32
Fig. 3.2 Mode shape convergence in terms of the elements used	33
Fig. 3.3 Bode diagram of the fuselage transfer function	35
Fig. 3.4 Mode shape of the local fuel tank modes.....	39
Fig. 3.5 Feedline geometry for the fuselage analysis	41
Fig. 3.6 Transfer function for the fuselage regarding two feedline configurations	43
Fig. 3.7 Geometric properties of the experiment [28].....	45
Fig. 3.8 Frequency spectrum of the pressure from the experiment [28]	45

Fig. 3.9 Frequency spectrum result for a T-shaped feedline.....	46
Fig. 3.10 Geometric properties of the present feedline	48
Fig. 3.11 Fluid compliance of unit length and area in terms of temperature...49	
Fig. 3.12 Bode diagram of the feedline modes in terms of the cavitation area(V_{cav}) at the pump inlet (feedline outlet) position	51
Fig. 3.13 Bode diagram of the feedline in terms of the friction factor.....	52
Fig. 3.14 Comparison of the feedline transfer function	55
Fig. 4.1 Comparison of the system frequency response function	57
Fig. 4.2 Sine sweep perturbation result of the closed loop response function	59

List of Symbols

Symbols	Meaning
δT	variation of the engine thrust
δr_{tank}	variation of the local displacement at tank
δQ_{LOX}	variation of LOX feedline volumetric flow rate
δP_{LOX}	variation of LOX feedline pressure
δq_{LOX}	perturbation of δQ_{LOX}
δp_{LOX}	perturbation of δP_{LOX}
$Q_{LOX,0}$	feedline-averaged volumetric flow rate
$P_{LOX,0}$	feedline-averaged pressure
f_{ij}	transfer function coefficients of the feedline characteristics
g_{ij}	transfer function coefficients of CFD meta model
h_{ij}	transfer function coefficients of LPRE
k_i	transfer function coefficients of the combustion equation
V_{cav}	cavitation volume
ϕ_n	fuselage structural mode
q_n	generalized coordinate
φ	local mode thrust position shape
φ_t	local tank mode shape
\hat{M}_{nn}	generalized mass
ζ_n	structural damping ratio
ω_n	natural frequency
σ_j	point source value of the fluid located at r_j
A_j	plane of action
e_{ij}	unit vector in the direction of the location i from j
p_i	MFLUID pressure
\dot{u}_i	MFLUID velocity

I_i	fluid inertance
$C_{f,i}$	fluid compliance
R_{fi}	fluid resistance
$[A]$	fluid inertance matrix
$[D]$	fluid resistance matrix
$[C]$	fluid compliance matrix
α_{LOX}	LOX thermal expansion coefficient
γ_{LOX}	LOX specific heat ratio
$C_{p,LOX}$	LOX heat capacity ratio at a constant pressure
q_{n_p}	generalized coordinate of the pressure
q_{n_q}	generalized coordinate of the volumetric flow rate
ω_{n_p}	eigenvalue of the pressure mode
ω_{n_q}	eigenvalue of the volumetric flow rate
ρ	density of the fluid
u	x -direction velocity of the fluid
p	pressure of the fluid
T	temperature of the fluid

Preface

This thesis is based on the following publications and manuscripts.

Journal 1

Park, K. J., Yoo, J. U., Lee, S. H., Nam, J. H., Kim, H. J., Lee, J. Y., Roh, T. - S., Yoh, J. J., Kim, C. A., Shin, S. J., "Pogo Accumulator Optimization Based on Multiphysics of Liquid Rockets and Neural Networks," *Journal of Spacecraft and Rockets*, Vol. 57, No. 4, July 2020, pp. 809-822.

Conference 1

Yoo, J. U., Park, K. J., Lee S. H., Shin, S. J., Design Optimization of a Pogo Suppression Device for Liquid Propulsion Rockets, *The 4th International Conference on Active Materials and Soft Mechatronics*, Incheon, 2019.

Conference 2

Yoo, J. U., Yoon, N. K., Lee S. H., Shin, S. J., " Pogo Analysis for a Clustered Rocket Engine by Sophisticated Branch-pipe Modeling," *2021 AIAA Sci-Tech Forum*, Virtual Forum, 2021. (To be presented)

The contents are reproduced with permission of the co-authors and the publishers. Copyright of the publications remains with the publishers.

Chapter 1

Introduction

1.1 Background

In the early development stage of rocketry, many space exploration mission vehicles were endangered by the longitudinal instability phenomenon known as pogo. Ever since the first occurrence in Thor/Agena and Titan II vehicles in the early 1960s, studies related to pogo have been carried out extensively [1-5]. Although many examinations have been conducted to a degree that the first elimination of pogo was successfully demonstrated in the Gemini launch vehicle, pogo analysis still remains an important task to be dealt with prior to every launch event.

Typically, a launch vehicle experiences such phenomenon when the pressure perturbations of LOX feedline causing thrust oscillations coincide with those of the fuselage along with fuel consumption. A commonly known solution is to separate the coinciding frequency intervals of the major components away, either smaller or larger, from the dominant longitudinal modes of the fuselage [6]. This may be easily achieved with the use of an accumulator in LOX feedline [7, 8]. However, in order to obtain accurate mode prediction for the fluid transmission line, sophisticated and realistic modeling for the feedline is required. Due to the fact that most launch vehicles nowadays are propelled by more than one liquid-propellant engine, acoustic modal response of a feedline

is significantly affected by a branch junction. Also, by the oscillation of the propellant flowing into the propulsion system such as the turbo-pump and the combustion chamber, each engine produces different thrust fluctuation with a certain degree of phase shift, which degrades the simplicity and certainty.

In fact, there are two types of oxidizer piping configuration for the first stage launch vehicle as illustrated in Fig. 1.1. An inner piping configuration where the oxidizer propellant flows through the center of the fuel tank is mainly used by a common bulkhead configuration, whereas the other is preferred by the tandem type where the feedline is installed exterior to the launch vehicle flowing individually into each engine. Ever since the first application in the first Soviet ICBM rocket R-36, common bulkhead fuel tank has been applied in many space launch vehicles mainly to reduce the piping weight and for the sake of various aerodynamic advantages. Although the common bulkhead does not necessarily represent any specific piping configuration to be chosen, branched feedline is required for the flow distribution to each engine. Nuri, a space launch vehicle currently under development in South Korea, has a tandem tank configuration with separate oxidizer feeding system flowing into each clustered rocket as shown in Fig. 1.2 [9]. While keeping this in mind, differences in the response will be investigated in the present thesis.

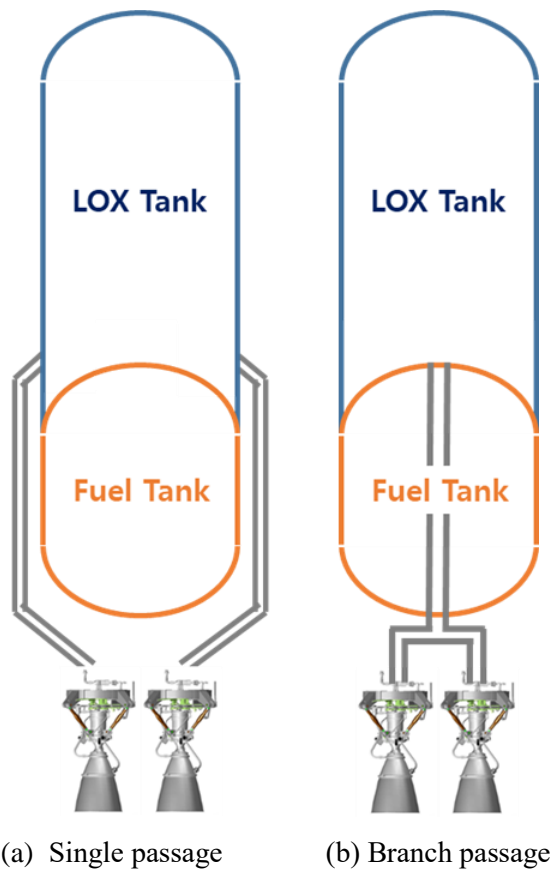


Fig. 1.1 Various configurations of LOX feedline

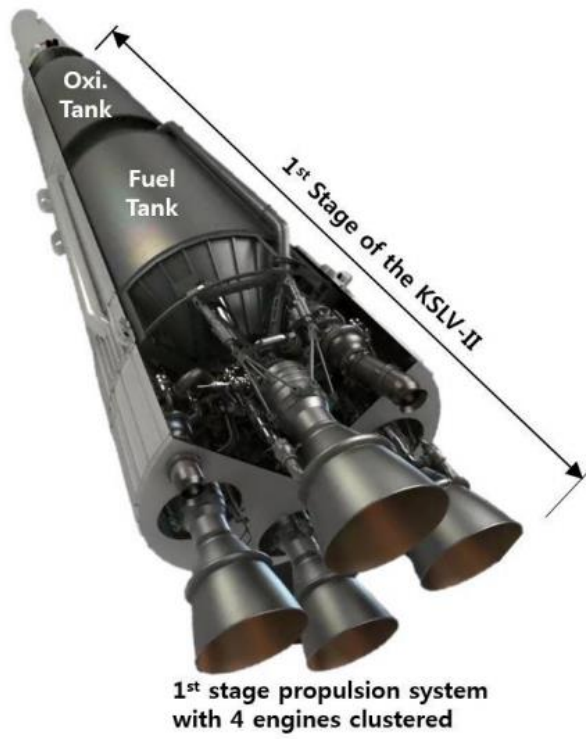


Fig. 1.2 Clustered rocket system of KSLV-II [9]

1.2 Previous Examinations

1.2.1 Fuselage Analysis

Complete system analysis for pogo instability was conducted by Rubin [10-12] and was further developed by Oppenheim [13]. The lumped parameter method suggested by Rubin and Oppenheim has been used widely in launch vehicle instability analysis, and it provided accurate pogo predictions. Zhao [14] and Wang [15] recently added improvements in pogo modeling by applying the lumped parameter methods. It is well known that the lumped parameter methodology is capable of accurately predicting the natural frequencies of a launch vehicle. However, the method cannot reproduce the system response precisely, resulting in discrepancy between the analysis and the experimental results. For such reasons, system analysis with the lumped parameter methodology may produce significantly conservative designs.

In addition, one- or two-dimensional modeling of a space launch vehicle regarding pogo analysis have been conducted [16, 17]. Recently, approaches utilizing three-dimensional model for pogo analysis have been carried out [18]. However, specific characteristics of the three-dimensional structural modes, which in fact vary in type, are not taken into account. Such results are compared with those by the high-fidelity fuselage analysis developed in this thesis.

1.2.2 Feedline Analysis

Up to date, branch pipe flow distribution problems have also been studied extensively by many researchers. Bajura [19] suggested an analytical technique

for the flow problems with dividing and combining manifold system. Reimann [20] studied the flow characteristics with regard to the pressure fluctuation occurring in a T-junction with experimental results. Xie [21] analyzed the effect of the five-way spherical cavity on flow distribution and also provided experimental results. He mentioned that non-constant pressure reduction occurred in a branched feedline system due to symmetric vortex state. In addition, branch pipe flow distribution problems with the use of cryogenic propellant have also been studied widely. Especially, Japanese H-IIB rocket used the liquid oxygen supply system to flow out separately from the tank in order to avoid interference between the two [22]. Korean sounding rocket-III (KSR-III) supply pipeline was designed to feed a limited amount of propellant from the tank during combustion, mainly to regulate the pressure fluctuations during ignition [23].

Although many researches regarding the branch-pipe flow in cryogenic launch vehicles have been conducted, not many literatures were reported regarding the pogo instability owing to branch-pipe induced flow distribution problems. In this thesis, complex LOX feedline system is to be modeled by one-dimensional lumped formulation using the analytic fluid transients and eigen solution techniques suggested by Michalopoulos [24]. Pressure modes of the two-way branch-pipe are to be analyzed and the equivalent transfer function is extracted to give a closed loop system for a clustered liquid rocket launch vehicle.

Chapter 2

Pogo Analysis Formulation

The process for analyzing pogo stability of a clustered liquid rocket is shown in Fig. 2.1. For each of the subsystem block illustrated in the figure, major characteristics of the launch vehicle are analyzed in the form of transfer function. The main variables of the system include the pressure and volumetric flowrate perturbation in the branch pipe feedline, thrust produced by the propulsion system, and the longitudinal displacement of the fuselage structure.

Transfer functions of the launch vehicle fuselage response are obtained accounting for the amount of fuel remaining in the tank. Since the vibration of the fuselage causes the longitudinal motion, the feedback vibrations are transmitted back to the inlet of the branch pipe feedline. Then the two exits of the feedline are connected in parallel with the combination of liquid propellant rocket engine (LPRE) and a combustor. Since the thrust oscillations of the engine again feedback the fuselage structural vibration, the entire process is a closed loop system. Classical pogo instability is found between the feedline pressure/volume flow mode and the fuselage vibration.

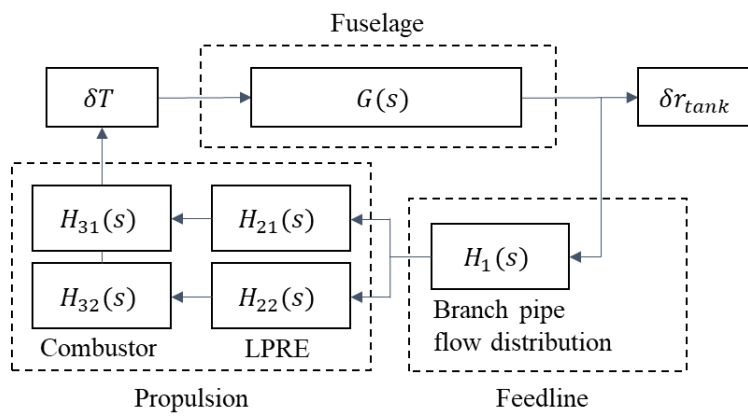


Fig. 2.1 Numerical integration procedure for a clustered engine rocket

2.1 Fuselage-Feedline Dynamic System

In this section, the major dynamics of the longitudinal system are specified to construct the numerical model. The interfaces for the dynamics are joined to form a complete closed loop system, and the transfer-function synthesis is used to obtain the response. Figure 2.2 shows the process for analyzing the longitudinal instability. The main variables introduced in the figure are thrust, displacement, pressure, and volumetric flow rate. By post-processing each analysis, the transfer function will be obtained in terms of the aforementioned variables.

If the subsystem formulation is single-input single-output (SISO), the transfer function is simply configured in a series connection. In the case of the multi-input multi-output (MIMO) subsystem, additional coupling terms should be considered. In the fuselage structural analysis, δT and δr_{tank} are connected in series, and the formulation is expressed in Eq. (1).

$$\frac{\delta r_{tank}}{\delta T} = f_{struct}(\phi_1, \phi_2, \dots, \phi_{N_s}) \quad (1)$$

where ϕ_j is the j^{th} fuselage mode. The tank displacement is distributed into the feedline pressure $P_{LOX,in}$ and the volumetric flow rate $Q_{LOX,in}$ components.

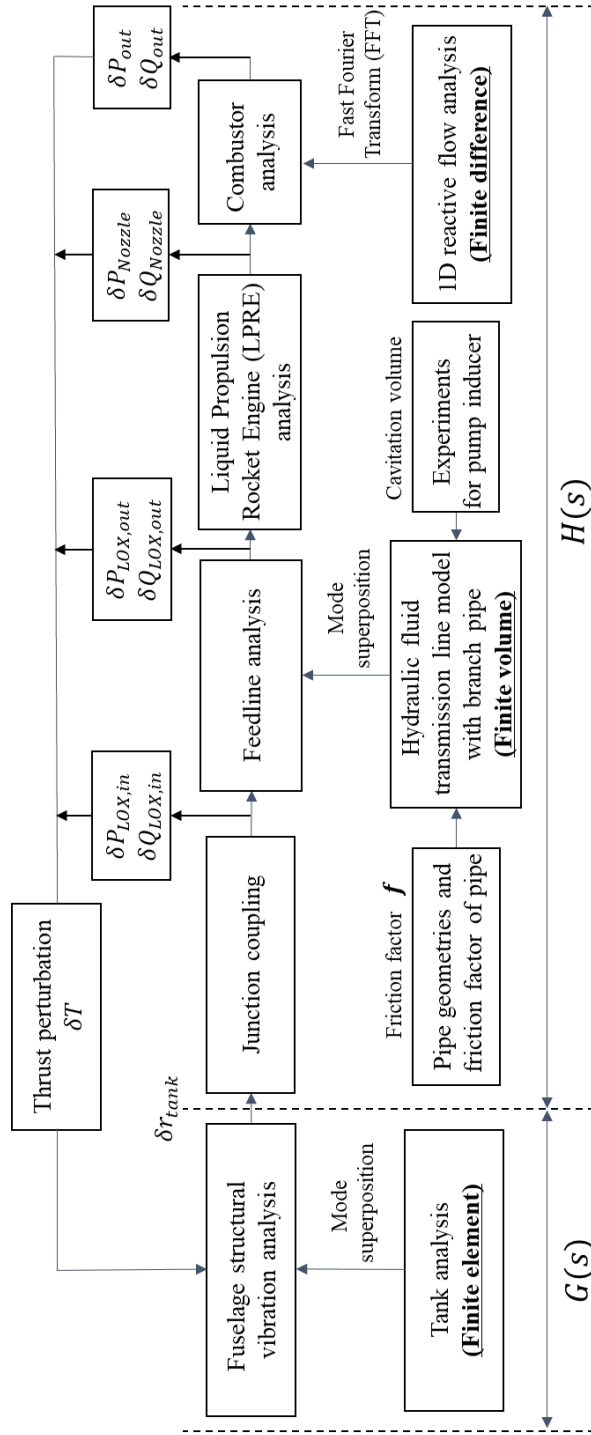


Fig. 2.2 Integrated procedure for pogo analysis for a liquid propulsion rocket

For each element, assuming small perturbation,

$$\delta P_{LOX} = P_{LOX,0} + \delta p_{LOX}, \quad \delta p_{LOX} \ll P_{LOX,0} \quad (2)$$

$$\delta Q_{LOX} = Q_{LOX,0} + \delta q_{LOX}, \quad \delta q_{LOX} \ll Q_{LOX,0} \quad (3)$$

where $P_{LOX,0}$ and $Q_{LOX,0}$ are the feedline-averaged pressure and volumetric flow rate, respectively. The perturbation of LOX feedline pressure and volumetric flow rate can be expressed as shown in Eq. (4).

$$\delta p_{LOX,in} = 0, \quad \delta q_{LOX,in} = A_{fin} \delta \dot{r}_{tank} \quad (4)$$

Equations (2) and (3) can be used for the pressure mode analysis and volumetric flow rate modal analysis, respectively. A transfer matrix is constructed for the pressure and volumetric flow rate at the outlet after passing through the feedline. The transfer matrix is shown in Eq. (5).

$$\begin{bmatrix} \delta p_{LOX,out} \\ \delta q_{LOX,out} \end{bmatrix} = \begin{bmatrix} f_{11} & f_{12} \\ f_{21} & f_{22} \end{bmatrix} \begin{bmatrix} \delta p_{LOX,in} \\ \delta q_{LOX,in} \end{bmatrix} \quad (5)$$

where f_{ij} is the transfer function determined from the feedline characteristics. The outlet of the LOX feedline joins with the inlet of the pump inducer, and the flow through the pump can be expressed as follows.

$$\begin{bmatrix} \delta P_{pump,out} \\ \delta Q_{pump,out} \\ V_{cav} \end{bmatrix} = \begin{bmatrix} g_{11} & g_{12} \\ g_{21} & g_{22} \\ g_{31} & g_{32} \end{bmatrix} \begin{bmatrix} P_{LOX,0} + \delta p_{LOX,out} \\ Q_{LOX,0} + \delta q_{LOX,out} \end{bmatrix} \quad (6)$$

g_{ij} is the transfer function of the meta model derived from CFD analysis, and V_{cav} is the cavitation volume of the feedline. The feedline performance depends heavily on the cavitation, meaning that f_{ij} depends on the cavitation

volume. Meanwhile, the numerical formation of pressure and volumetric flow rate of the pump outlet LOX feedline include components such as the turbine and injector. After passing through the LPRE equation, the following relations for the combustor will be obtained.

$$\begin{bmatrix} \delta p_{Combustor} \\ \delta q_{Combustor} \end{bmatrix} = \begin{bmatrix} h_{11} & h_{12} & h_{13} & h_{14} \\ h_{21} & h_{22} & h_{23} & h_{24} \end{bmatrix} \begin{bmatrix} \delta P_{LOXpump,out} \\ \delta Q_{LOXpump,out} \\ P_{Fuelpump,out} \\ Q_{Fuelpump,out} \end{bmatrix} \quad (7)$$

where h_{ij} is LPRE transfer function. Using the pressure and volumetric flow rate of the combustor, thrust can be induced as shown in Eq. (8).

$$\delta T = [k_1 \quad k_2] \begin{bmatrix} \delta p_{Combustor} \\ \delta q_{Combustor} \end{bmatrix} \quad (8)$$

k_i is the transfer function of the combustion formulation. Since the thrust perturbation is fed back into the thrust itself, pogo instability will be determined by observing the attenuation. Here, the different transfer functions can be combined depending on the numerical formulation. Alternatively, a meta model of the transfer function through FFT can be extracted for the case of nonlinear analysis. Numerical modeling is performed using the specific geometry, and the relevant transfer function is obtained to derive the entire system. The pogo system composed of the numerical analysis allows for the observation of the frequency response function (FRF) depending on the geometric design. In the following sections, the coefficients within each transfer function will be defined.

2.2 Fuselage Transfer Function $G(s)$

Since the fuselage frequency response function f_{struct} in Eq. (1) is a transfer function of thrust δT and local displacement δr_{tank} , the rational function form can be obtained by analyzing the dynamic response. In order to accurately interpret the response of the feedline inlet pressure and volumetric flow rate, detailed modeling of the local parts can be performed to improve the accuracy of the dynamic response.

For baseline of the fuselage components, Atlas-Centaur-Surveyor mass-spring representation is used [13]. The representation is reproduced with detailed modeling of the propellant tanks and the near-by components, producing one- and three-dimensional integrated representation based on the experimental results [25]. Accurate mode shape is captured by the present detailed modeling and is considered to improve the accuracy of the transfer function.

One- and three-dimensional representations are acquired with the detailed geometry as shown in Fig. 2.3. Based on Atlas-Centaur launch vehicle, LOX and fuel tanks are modeled in high-fidelity, and the remaining components are modeled as lumped mass accordingly. Element refinement is performed by the local refinement algorithm of element density increase ratio of 1:3. Also, the effects on the response are observed for both cases where the feedline is physically attached to the interior and exterior of the tank structures. The transfer functions for both single and branch passage are derived for comparison.

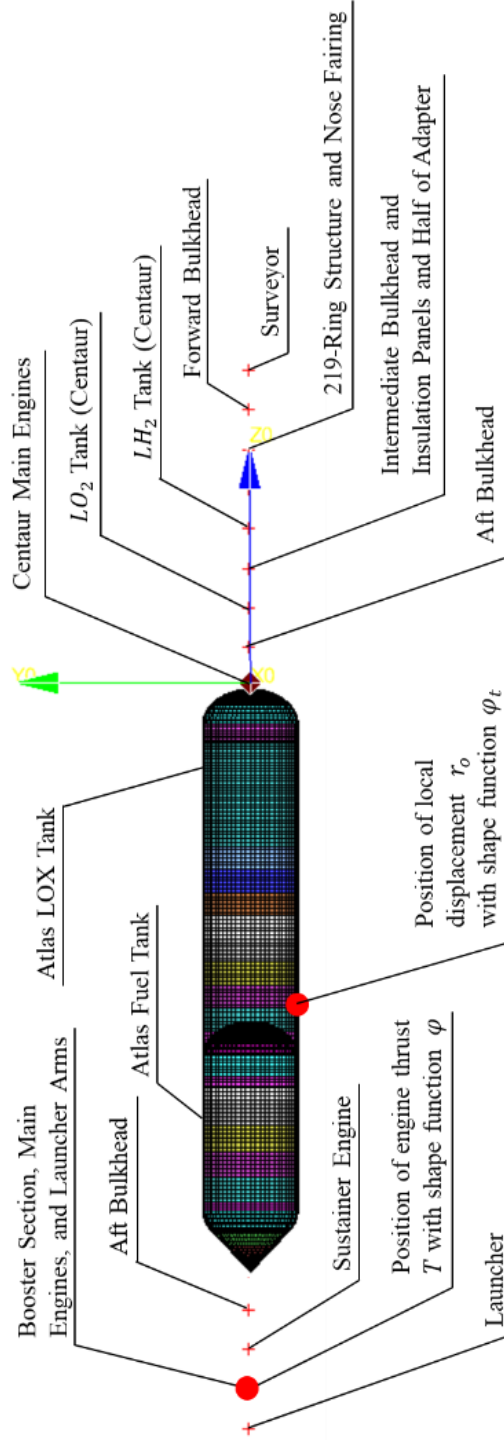


Fig. 2.3 Finite element model based on Atlas launch vehicle

Formulation of finite element analysis used for the fuselage representation is written in Eq. (9).

$$[M]\{\ddot{r}_i\} + [C]\{\dot{r}_i\} + [K]\{r_i\} = [T_i] \quad (9)$$

The mass matrix $[M]$, damping matrix $[C]$ and stiffness matrix $[K]$ are obtained using NASTRAN QUAD4 element. $[T_i]$ is the force vector, and $\{r_i\}$ is the displacement vector. The top dot stands for the derivative with respect to time t . Generalized eigenvalue analysis is performed in Eq. (10).

$$[-\omega_n^2 M + K]\{\varphi_{ni}\} = 0 \quad (10)$$

By the modal analysis, eigenvalues ω_n and the corresponding eigenvectors $\{\varphi_{ni}\}$ will be obtained. It is worth noting that the analysis results are estimated from the lowest modes and contain modes with different characteristics. However, pogo instability is mainly influenced by the longitudinal modes only. For an efficient analysis, reduced order model may be constructed by setting an influence vector $\{d\}$ for appropriate system and assessing the modal participation factor.

The system generalized mass matrix is written in Eq. (11)

$$[\hat{M}] = [\phi^T][M][\phi] \quad (11)$$

Coefficient vector \bar{L} is written in Eq. (12)

$$\bar{L} = [\phi^T][M]\{d\} \quad (12)$$

Modal participation vector Γ_i can be computed in Eq. (13).

$$\Gamma_i = \frac{\bar{L}_i}{\hat{M}_{ii}} \quad (13)$$

Using the influence vector $\{d\}$, effective modal mass on i^{th} mode will be written in Eq. (14).

$$m_{eff,i} = \frac{\bar{L}_i^2}{\hat{M}_{ii}} \quad (14)$$

To sort out the longitudinal modes, $\{d\}$ can be obtained by the following static analysis.

$$[K]\{d\} = \{f\} \quad (15)$$

where $F_{6i} = 0, F_{6i+1} = 0, F_{6i+2} = 1, F_{6i+3} = 0, F_{6i+4} = 0, F_{6i+5} = 0$ for the i^{th} node. From $\{d\}$ of the i^{th} effective modal mass $m_{eff,i}$, pogo-critical fuselage mode will be obtained.

For N longitudinal eigenvalues, reduced mode amplitude r_o can be expressed as the sum of generalized coordinate q_n and eigenvector in Eq. (16).

$$r_o = \sum_{n=1}^N \varphi_{no} q_n \quad (16)$$

If the fuselage contains structural damping, response on the n^{th} longitudinal mode will be expressed in Eq. (17).

$$\hat{M}_{nn}(\ddot{q}_n + 2\zeta_n\omega_n\dot{q}_n + \omega_n^2q_n) = Q_n(t) \quad (17)$$

where ζ_n is the damping ratio, ω_n is the natural frequency, and Q_n is the generalized force on the fuselage which is the thrust.

To assess an open loop system, response due to a random input should be examined. Expanding on an excitation point and frequency domain, Q_n will be expressed in Eq. (18).

$$Q_n = \sum_{i=1}^{N_{dof}} T_i(e_i \cdot \varphi_{nj}) = \sum_{i=1}^{N_{dof}} T_i \varphi_{ni} \quad (18)$$

Equation (17) is a multi-input-multi-output (MIMO) system. To evaluate the transfer function to single-input-single-output (SISO), the only input will be assumed to be the thrust of the engine. Putting i as the longitudinal deflection degree of freedom of the engine, $i = I, I \in 1 \leq i \leq N_{dof}$ will be satisfied, leading to Eq. (19).

$$Q_{n,engine} = T_I \varphi_{nI} \quad (19)$$

For N longitudinal modes and force T_I acting on the i^{th} degree of freedom, generalized force can be computed as follows. Assuming $T_I = T_{input}$, equation of the system will be simplified as shown in Eq. (20).

$$\widehat{M}_{nn}(s^2 q_n + 2\zeta_n \omega_n s q_n + \omega_n^2 q_n) = T_{input} \varphi_{nI} \quad (20)$$

Fuselage structural response on thrust excitation is the transfer function on SIMO system, as shown in Eq. (21).

$$\frac{q_n}{T_{input}} = \frac{\varphi_{nI}}{\widehat{M}_{nn}(s^2 + 2\zeta_n \omega_n s + \omega_n^2)} \quad (n = 1, 2, \dots, N) \quad (21)$$

By connecting multiple transfer functions in parallel, the transfer function will be converted to SISO form as Eq. (22).

$$\frac{\delta r_o}{\delta T_{input}} = \sum_{n=1}^N \varphi_{no} \frac{\delta q_n}{\delta T_{input}} = \sum_{n=1}^N \frac{\varphi_{ni} \varphi_{no}}{\widehat{M}_{nn}(s^2 + 2\zeta_n \omega_n s + \omega_n^2)} \quad (22)$$

In Eq. (22), o denotes the oxygen feedline inlet position, where the point in which the displacement is obtained. In the mass spring representation, main transfer function is obtained on the center of mass of the main component. On the contrary, for finite element, detailed displacement will be acquired. This will lead to improved results of the mode shapes φ_{ni} , φ_{no} and scaling of the transfer function.

In addition, as fuel is consumed in the launch vehicle, the remaining fuel level will decrease, thereby changing the characteristics of the entire fuselage. By this consideration, it will be necessary to account for the hydro-elastic effect variation as a result of LOX and fuel consumption. This may be achieved by the virtual mass method implemented in MFLUID element of NASTRAN. The fluid mass matrix is constructed by the pressure and velocity derived by the following equations.

$$p_i = \sum_j \int_{A_j}^d \frac{\rho \dot{\sigma}_j e_{ij}}{|r_i - r_j|} dA_j \quad (23)$$

$$\dot{u}_i = \sum_j \int_{A_j}^d \frac{\sigma_j e_{ij}}{|r_i - r_j|^2} dA_j \quad (24)$$

where σ_j is the point source value of the fluid located at r_j , A_j is the plane of action, and e_{ij} is the unit vector in the direction of the location i from the

location j . MFLUID will be used to estimate the changes in the fuselage structural frequencies in terms of the fuel level.

2.3 Feedline Transfer Function $H(s)$

Numerical analysis for f_{ij} defined in Eq. (5) will be carried out by the feedline containing the branch-pipe configuration. The acoustic modes of the cryogenic propellant in sophisticated fluid networks are analyzed using the one-dimensional flow network transmission line formulation [26]. The formulations were built upon the following assumptions: steady flow, irrotational inviscid flow, incompressible flow, streamline identical to the pathline, and negligible convection.

Based on the finite element analysis, the pipeline is divided into several elements and the corresponding inertance I_i , compliance C_i , and resistance $R_{f,i}$. Equation (25) is derived from the one-dimensional momentum equation while ignoring the convection term, and Eq. (26) is the conservation of mass equation when assuming an adiabatic liquid flow.

$$I_i \dot{Q}_i = P_i - P_{i+1} - R_{f,i} |Q_i^0| Q_i \quad (25)$$

$$C_{f,i} \dot{P}_i = Q_{i-1} - Q_i \quad (26)$$

where the symbols are defined as:

$$\text{Inertance } I_i = \frac{\rho_{LOX} L_i}{A_i} \quad (27)$$

$$\text{Compliance } C_i = \frac{1}{K_{s,LOX}} = \frac{\alpha_{LOX} A L_i}{\gamma_{LOX} C_{p,LOX}} \quad (28)$$

$$\text{Resistance } R_{fi} = \frac{\rho_{LOX}}{2A_i^2} f \left(\frac{L_i + L_e}{D_i} \right) \quad (29)$$

Inertance in Eq. (27) is estimated by considering the geometry and density of the fluid. Resistance depends on the fluid density and friction factor of the pipe flow f . Compliance is modeled by adiabatic bulk modulus.

The thermal expansion coefficient α_{LOX} of the liquid oxygen used in the compliance term is defined as shown in Eq. (30). A well-known relation of the thermal expansion coefficient with respect to temperature is shown in Eq. (31) [27].

$$\alpha_{LOX} = \frac{1}{V} \left(\frac{\partial V}{\partial T} \right)_T \quad (30)$$

$$10^6 \cdot 3\alpha_{LOX} = 51.03 + 0.66 \left(\frac{T}{100} \right) - 3.18 \left(\frac{T}{100} \right)^2 \quad (31)$$

The temperature of the liquid oxygen inside the feedline ranges from 90K to 108K. Figure 2.4 shows the temperature/heat capacity in terms of pressure inside the pipe. It is observed that the numerical values of the heat capacity deviate from the trend rapidly at low pressure operating condition.

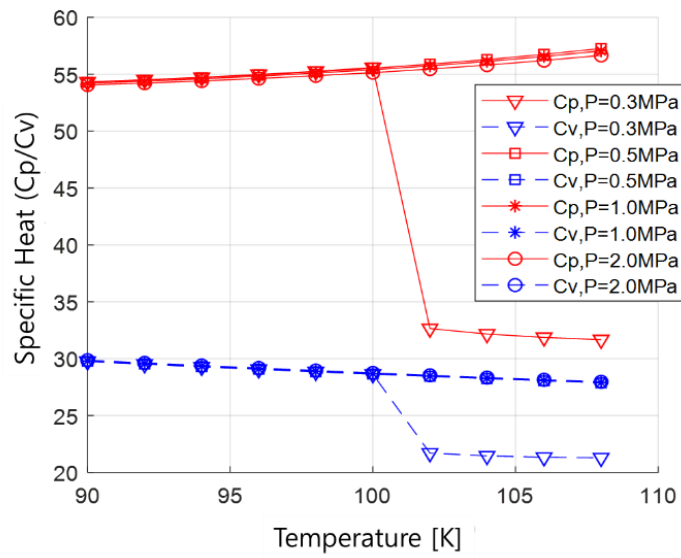


Fig. 2.4 Constant pressure/volume heat capacity for the present operating pressure and temperature

Equations (25) and (26) are nonlinear equations, but they may be linearized by implementing the small perturbation hypothesis mentioned in Eqs. (2) and (3). Equations (32) and (33) give the results of the volumetric flow rate and pressure decoupled by the small perturbation assumptions.

$$[A]\ddot{q} + [D]\dot{q} + [E_Q]q = h_1 \quad (32)$$

$$[C]\ddot{p} + [H]\dot{p} + [E_P]p = h_2 \quad (33)$$

where $[A]$, $[D]$, $[C]$ are the inertance, resistance, and compliance matrices, respectively, with diagonal elements.

$$[C] = \begin{bmatrix} C_1 & 0 & 0 & 0 \\ 0 & C_1 & 0 & 0 \\ 0 & 0 & \ddots & 0 \\ 0 & 0 & 0 & C_1 \end{bmatrix} \quad (34)$$

$$[A] = \begin{bmatrix} I_1 & 0 & 0 & 0 \\ 0 & I_1 & 0 & 0 \\ 0 & 0 & \ddots & 0 \\ 0 & 0 & 0 & I_1 \end{bmatrix} \quad (35)$$

$$[D] = \begin{bmatrix} 2R_{f1}Q_1^0 & 0 & 0 & 0 \\ 0 & 2R_{f1}Q_1^0 & 0 & 0 \\ 0 & 0 & \ddots & 0 \\ 0 & 0 & 0 & 2R_{f1}Q_1^0 \end{bmatrix} \quad (36)$$

where $I_i = \frac{\rho_{LOX}L_i}{A_i}$, $R_{fi} = \frac{\rho_{LOX}}{2A_i^2} f \left(\frac{L_i+L_e}{D_i} \right)$, $C_i = \frac{1}{K_{s,LOX}} = \frac{\alpha_{LOX}A_i}{\gamma_{LOX}c_{p,LOX}}$ and

consist of the element length L_i , cross-sectional area A_i of the element, density of the fluid ρ_{LOX} , diameter of the tube D_i , and the friction factor f . These parameters can be obtained from the fluid properties and the geometry of the pipeline.

Figure 2.5 shows the overall configuration of the branch-pipe by the two-way junction modeling.

With the three fluid transients mentioned in Eqs. (27)-(29) defined for each element, geometric matrix B can be obtained using the following relation in Eq. (37). Taking the configuration in Fig. 2.5 as an example, the element will be numbered in order until K element leading to the first LOX pump rejoins the junction element into the inlet of the second branch pipe.

$$[B] = \begin{bmatrix} -1 & 1 & 0 & 0 & 0 & 0 \\ 0 & -1 & 1 & 0 & 0 & 0 \\ 0 & 0 & -1 & 1 & 0 & 0 \\ & & & \ddots & & \\ 0 & -1 & 0 & 0 & -1 & 1 \\ 0 & 0 & 0 & 0 & 0 & -1 \end{bmatrix} \quad (37)$$

$$B_{i \ i} = -1; \ i = 1 \sim N; \ i \neq k$$

$$B_{kj} = -1$$

$$B_{i \ i+1} = 1; \ i = 1 \sim N - 1$$

Also, $[E_Q]$ and $[E_P]$ are expressed as the product of the pipe geometry and the diagonal matrix as follows.

$$[E_Q] = [B][C^{-1}][B^T] \quad (38)$$

$$[E_P] = [B^T][A^{-1}][B] \quad (39)$$

Since all the above matrices are symmetric, Eq. (38) for the volumetric flow rate may easily be diagonalized by the modal analysis.

h_1 and h_2 are presented in Eqs. (40) and (41).

$$h_1 = \dot{f}_1 - [B][C^{-1}]f_2 \quad (40)$$

$$h_2 = \dot{f}_2 + [B^T][A^{-1}](f_1 + [D][B^T]^{-1}f_2) \quad (41)$$

where $f_1 = \begin{bmatrix} Q_0 \\ 0 \\ \vdots \\ 0 \end{bmatrix}$ and $f_2 = \begin{bmatrix} 0 \\ 0 \\ \vdots \\ -P_N \end{bmatrix}$. $[H]$ can be expressed as below.

$$[H] = [B^T][A^{-1}][D][B^T]^{-1}[C] \quad (42)$$

Since $[H]$ matrix is asymmetric as shown in Eq. (43), the derivation will be a complicated process. While the generalized solution of the undamped pressure mode is obtained by the eigenvalue analysis, non-classical asymmetric and non-diagonal damping matrix will be considered for the branched pipeline. The criteria for the damping matrix are shown in Table 1. The table also shows the application and examples.

Table 1 Types of the damping matrix and application

Matrix Type	Application	Example
Diagonal damping matrix	Flow rate analysis of simple feedline	Simple feedline
Diagonally dominant damping	Pressure perturbation analysis of feedline with low complexity	Feedline with varying cross-section: Linear increase/decrease model of diagonal components Inertance, Compliance, Resistance (ICR)
Non-classical symmetric damping	Flow rate analysis of complicated branch pipe feedline	Effect of system cooling condition (temperature); Nonlinear increase/decrease model of diagonal components of ICR
Non-classical asymmetric damping	Pressure perturbation analysis of complicated branch pipe feedline	Consideration of sophisticated pipeline with junctions such as branch pipes or pogo suppression devices

Since the formulation can be treated as a quadratic eigenvalue problem(QEP), its solution will be obtained by a direct method called QZ algorithm.

$$[H]^T = ([B^T][A^{-1}][D][B^T]^{-1}[C])^T = [C]^T[B^{-1}][D]^T[A^{-1}]^T[B] \neq [H] \quad (43)$$

$$Q(\lambda) = \lambda^2[C] + \lambda[H] + [E_p] \quad (44)$$

The generalized coordinates, eigen pairs of the pressure mode, and the volumetric flow rate are expressed as q_{n_p} ($\omega_{n_p}, \sum_{i=1}^{N_p} x_{i,n_p}$) and q_{n_q} ($\omega_{n_q}, \sum_{i=1}^{N_q} x_{i,n_q}$), respectively. The solution for the pressure and volumetric flow rate at the feedline inlet/outlet will be obtained as follows.

$$q_{LOX,out} = \sum_{n_q=1}^{N_q} x_{n_q,N_q} q_{n_q}, \quad q_{LOX,in} = \sum_{n_q=1}^{N_q} x_{n_q,1} q_{n_q} \quad (45)$$

$$p_{LOX,out} = \sum_{n_p=1}^{N_p} x_{n_p,N_p} q_{n_p}, \quad p_{LOX,in} = \sum_{n_p=1}^{N_p} x_{n_p,1} q_{n_p} \quad (46)$$

The generalized coordinate is obtained by the following equations.

$$\left(\hat{A}_{n_q n_q} s^2 + \hat{D}_{n_q n_q} s + \omega_{n_q}^2 \right) q_{n_q} = H_1(s) \quad (47)$$

$$\left(\hat{C}_{n_p n_p} s^2 + \hat{H}_{n_p n_p} s + \omega_{n_p}^2 \right) q_{n_p} = H_2(s) \quad (48)$$

$H_1(s)$ and $H_2(s)$ are Laplace transform of $h_1(t)$ and $h_2(t)$, respectively.

When the pump cavitation occurs, bubbles are generated at the feedline outlet, which will affect the compliance and inertance terms. Using the rule of the mixtures approach, the cavitation volume at the outlet can be reflected in Eqs.

(49) and (50).

$$I_{cav} = \frac{\rho_{LOX,liquid} L_i}{A_i} (1 - V_{cav}) + \frac{\rho_{LOX,air} L_i}{A_i} V_{cav} \quad (49)$$

$$C_i = \frac{1}{K_{s,LOX}} (1 - V_{cav}) + \frac{A_i L_i}{\rho_{LOX,air} c^2} \quad (50)$$

where c is the speed of the sound in oxygen gas, and V_{cav} is the ratio of the cavitation volume to the element volume.

From this analysis, and by including the feedline geometry information, the transfer function will be formulated. Depending on the location and the number of branching sections, the inertance, compliance, and resistance of the entire system will be affected, which will then affect the transfer function $H(s)$.

2.4 Combined Transfer Function

To link the two transfer functions of the aforementioned response analyses, relationship between the fuselage resultant displacement and the feedline modes should be investigated.

Pressure at the bottom of LOX tank, which is equivalent to the feedline input volumetric flow rate, can be obtained as Eq. (51).

$$\delta Q_{fin} = A_{fin} \delta \dot{r}_o \quad (51)$$

where δQ_{fin} is the feedline inlet volume flow rate and A_{fin} is the area of feedline inlet. By taking Laplace transform of Eq. (51), Eq. (52) will be obtained.

$$\frac{\delta Q_{fin}}{\delta r_o} = A_{fin} s \quad (52)$$

The open loop transfer function of the fuselage-feedline is written in Eq. (53).

$$G(s) = \frac{\delta Q_{fout}}{\delta T_{input}} = \frac{\delta Q_{fout}}{\delta Q_{fin}} \frac{\delta Q_{fin}}{\delta r_o} \frac{\delta r_o}{\delta T_{input}} \quad (53)$$

Substituting the relevant functions, $G(s)$ can be written in Eq. (54).

$$G(s) = \sum_{n=1}^N \sum_{n_Q=1}^{N_Q} \frac{s^2 A_{fin} x_{n_Q,N} x_{n_Q,1} \varphi_{nI} \varphi_{no}}{\widehat{M}_{nn} (s^2 + 2\zeta_n \omega_n s + \omega_n^2) (\widehat{A}_{n_Q n_Q} s^2 + \beta_{n_Q n_Q} s + \omega_{n_Q}^2)} \quad (54)$$

Equation (54) is the combined transfer function from the fuselage response and the feedline volumetric flowrate mode. This function will be amplified by four parameters $(x_{n_Q,N}, x_{n_Q,1}, \varphi_{nI}, \varphi_{no})$ for every combination of the fuselage and feedline modes. Assuming infinite number of modes ($N \rightarrow \infty, N_Q \rightarrow \infty$), contribution of each mode to transfer function $G(s)$ will be negligible as it is proportional to multiplication of fuselage mode $\varphi_{nI} \varphi_{no} / \widehat{M}_{nn}$ and pressure mode $x_{n_Q,N} x_{n_Q,1} / \widehat{A}_{n_Q n_Q}$.

For the single passage configuration, the location of the fuselage resultant node is modified from the bottom to the side of LOX tank, where it joins with the single passage feedline inlet. The cross-sectional area of the feedline expressed in Eq. (51) will be also reduced to a smaller value to account for the difference of the feedline configuration.

Chapter 3

Verification and Application

3.1 Verification of the Fuselage Response

By the finite element model using one- and three-dimensional representations, various types of the fuselage modes may appear as shown in Table 2. Without the proper boundary condition, the first few modes will be the rigid body modes. Additional ones include the radial, circumferential, and shear modes. Among the first 1,000 modes, only 16 of them appear to be longitudinal, and thus the rest are limitedly related to pogo instability. Except for the longitudinal modes, every other mode shows coupled frequencies. To evaluate the system response, contribution factor of the longitudinal modes is assessed.

Modal participation factor described in Section 2.2 is investigated at the feedline inlet node. Rearranging the fuselage modes based on the modal participation factor, the first 10 modes shown in Table 3 contain 99% of the total effective mass. System analysis is performed by those 10 modes.

Difference of the eigenvector between the lumped parameter methodology and the high-fidelity representation is shown in Fig. 3.1. Although both provide similar shapes, the corresponding eigenvalues will clearly differ. In Fig. 3.2, modal shape change in terms of the element number is shown. The shapes are different depending on the location, and the mode shape of each node will converge as the number of elements increases. Thus the present high fidelity representation will improve the scaling accuracy of the transfer function.

Table 2 Types of the fuselage modes

Mode	Coupled	Mode	Coupled
Rigid	No	Axial bending	Yes
Pure radial	Yes	Global torsion	Yes
Radial with shearing	Yes	Global bending	Yes
Extensional	Yes	Global longitudinal	No
Circumferential	Yes	Local longitudinal	No

Table 3 Rearrangement of the longitudinal modes by the modal participation factor

Mode number	Natural frequency (Hz)	Original mode number (including coupled)	Participation factor for longitudinal displacement (%) from thrust
1	7.41	5,108	0.017
2	8.45	5,429	0.003
3	9.44	5,655	90.34
4	11.34	5,981	0.004
5	12.24	6,121	0.199
6	16.78	6,663	0.335
7	17.05	6,687	6.672
8	25.01	7,230	1.865
9	31.54	7,532	0.012
10	34.87	7,651	0.506
Sum			99.95

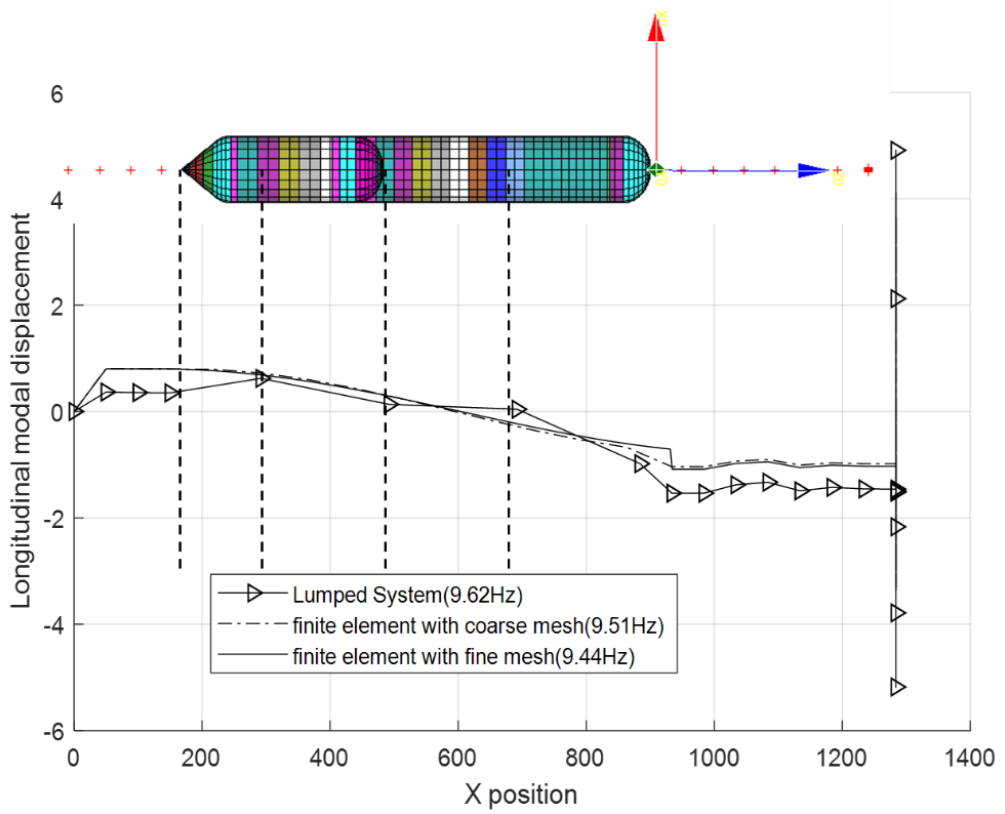


Fig. 3.1 Difference for the longitudinal modal displacement between the lumped and high-fidelity representation

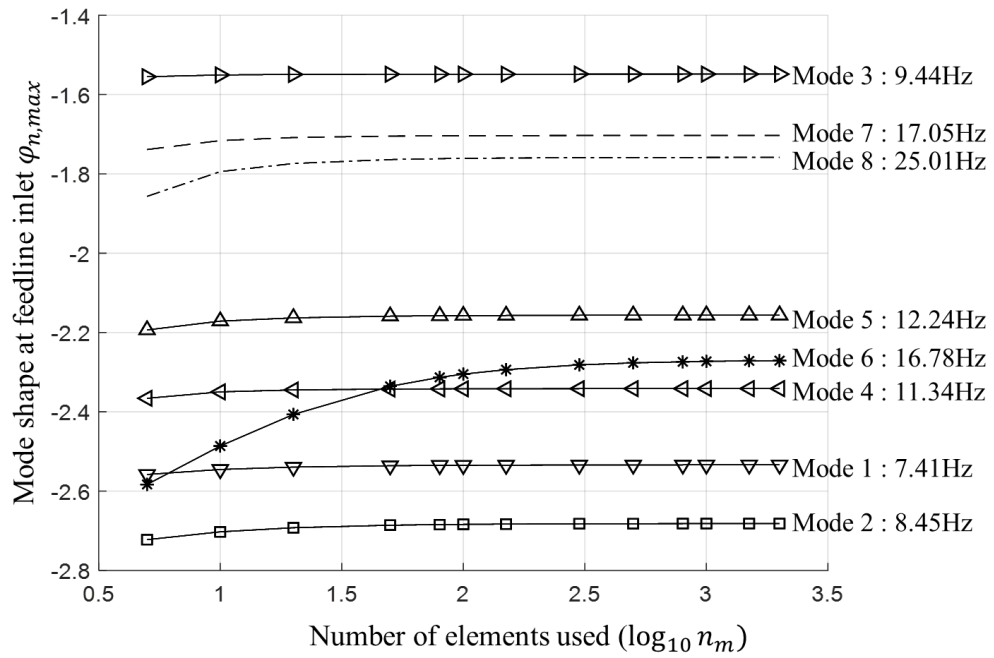


Fig. 3.2 Mode shape convergence in terms of the elements used

With the fuselage results described above, Bode plots based on the most influential modes are to be created comparing the lumped parameter and high fidelity representations. The result is shown in Fig. 3.3. The natural frequencies of the lumped parameter methodology are found to be quite accurate, showing little deviation from those by the high-fidelity representation as shown in Table 4. However, it is observed from Fig. 3.3 that the discrepancies arise with regard to magnitudes of the transfer function for the mode such as 31.5Hz. Such differences in the peak points of the transfer function may change the overall stability of the system when integrated with those of the feedline analysis.

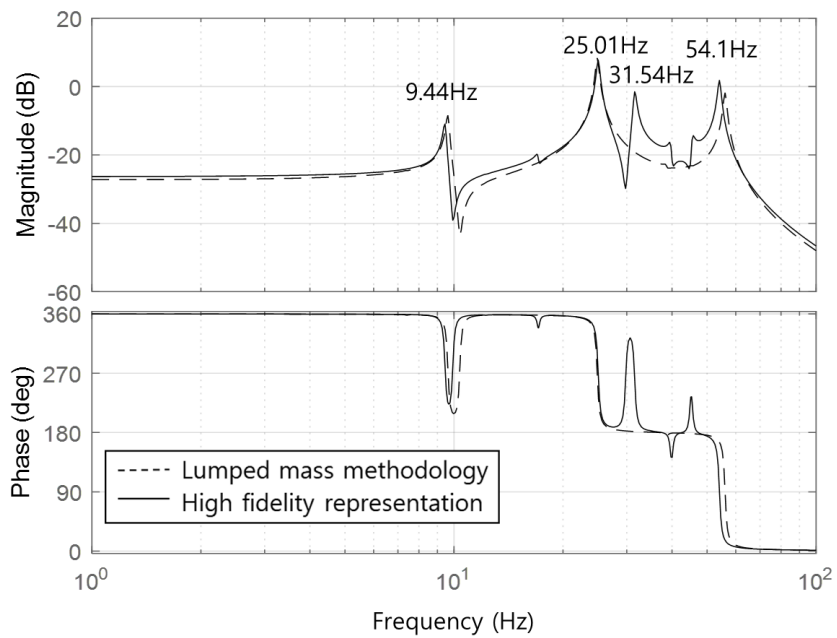


Fig. 3.3 Bode diagram of the fuselage transfer function by both lumped parameter methodology and high fidelity representation

Table 4 Comparison of the resonant frequencies by lumped parameter methodology and high fidelity representation

Mode number	Lumped parameter methodology		High fidelity representation		Difference (%)
	Resonant Frequency (Hz)	Peak Existence	Resonant Frequency (Hz)	Peak Existence	
3	9.6	o	9.4	o	-1.91
8	24.9	o	25.0	o	0.60
9	31.5	x	31.5	o	0.13
11	38.6	x	39.7	o	2.79
12	45.3	x	45.6	o	0.37
15	56.1	o	54.1	o	-3.64

Also, considering the fuel usage in the tank, hydroelastic characteristics of the tank will also be taken into account. Unlike the lumped parameter methodology, additional modes are found for the one- and three-dimensional combined representations. In addition to the global modes that have been analyzed by the lumped parameter methodology, two local modes with the resonant frequencies are found as shown in Table 5.

The modal participation factor of the fuselage modes is examined under the full fuel condition. The results show that modes under 30Hz display large correlation to the longitudinal dynamic characteristics of the launch vehicle. Those modes are depicted in boldface in Table 5. Especially, the first global mode, which rests in 9.4Hz, may be fatal to the pogo instability. The mode shapes of those local fuel tank modes are illustrated in Fig. 3.4.

As the mesh information becomes more detailed, additional local fuselage modes will be found. Also, such modes are considered to have a significant effect on the displacement of the feedline.

Table 5 Comparison of the dominant modes regarding the fuel balance dependency

1D original*		1D refined mass spring		3D refined finite element	
Frequency (Hz)	Fuel balance dependency	Frequency (Hz)	Fuel balance dependency	Frequency (Hz)	Fuel balance dependency
7.41	Weakly	7.41	Weakly	7.45	Weakly
8.45	Weakly	8.45	Weakly	8.50	Weakly
9.62	Strongly	9.44	Strongly	9.41	Strongly
11.34	Weakly	11.34	Weakly	11.41	Weakly
12.27	Weakly	12.24	Weakly	12.32	Weakly
16.79	Weakly	16.78	Weakly	16.88	Weakly
-	-	17.05	Strongly	16.49	Strongly
-	-	-	-	21.40	Strongly
24.86	Strongly	25.01	Strongly	26.85	Strongly
-	-	-	-	28.82	Strongly

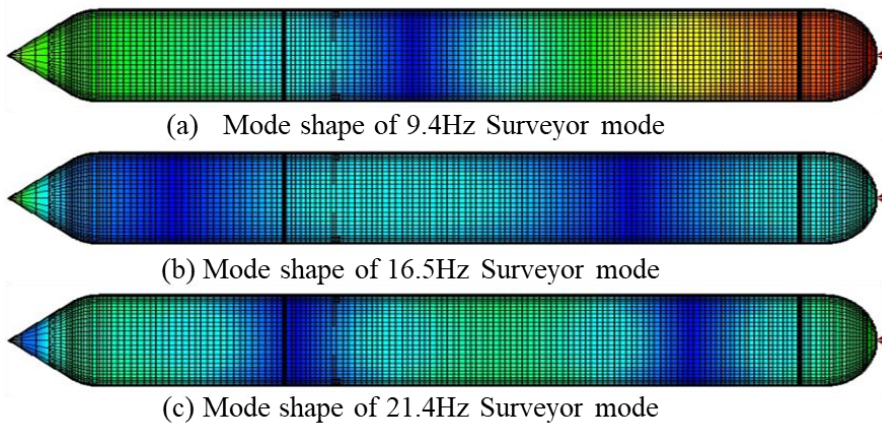
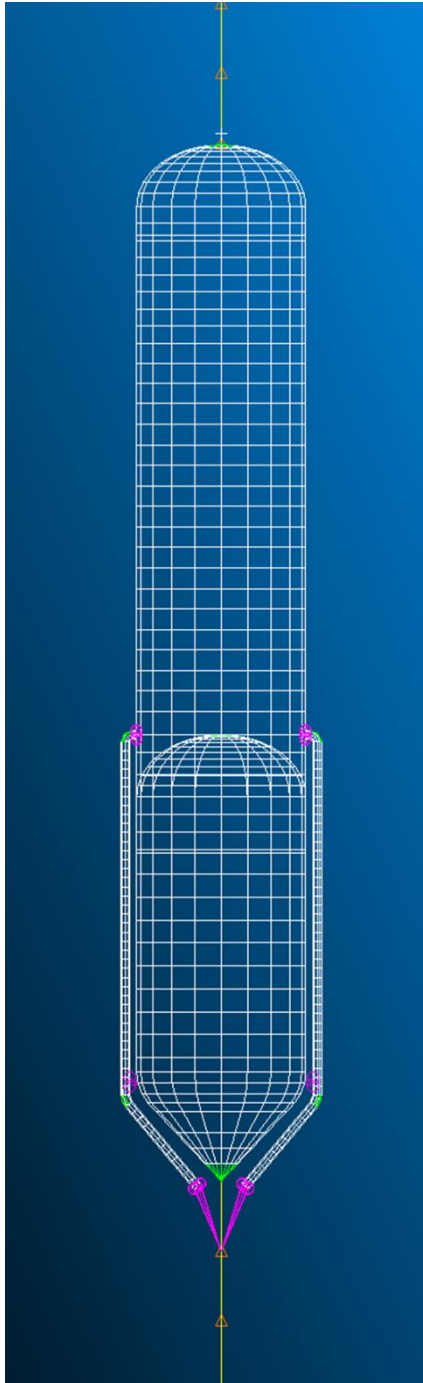


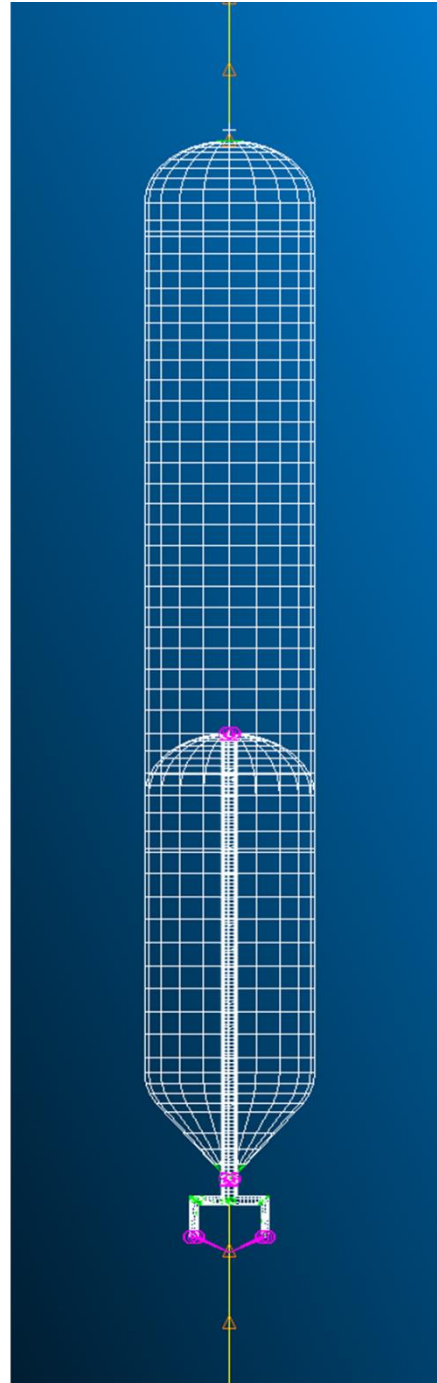
Fig. 3.4 Mode shape of the local fuel tank modes

In addition to the detailed representation of the propellant tanks, the geometry of the branch feedline will also be included in the formulation of the fuselage transfer function. Unlike a typical launch vehicle, the branch feedline in a launch vehicle with a common bulkhead requires that the main feedline should penetrate through the fuel tank under the oxidizer tank. Therefore, the change of the volume and weight may affect the response of the fuselage modes. For comparison of the fuselage response between the single and the branch passage configurations, the schematics are shown in Fig. 3.5.

The figure shows NASTRAN windows for two feedline configurations. Figure 3.5 (b) is the three-dimensional tank finite element representation with a branch passage feedline located in the fuel tank. On the other hand, (a) contains two single passage feedlines attached exterior to the oxidizer tank flowing individually into each engine. It is worth noting that the inlet of the single passage configuration has been modified from that of the branching passage. Also, due to the fact that the outlet of both feedlines connect with the engine, the nodes of the feedline outlets are connected to the lumped mass node of sustainer engine located right below the tank using RBE2 elements as colored in purple.



(a) Single passage



(b) Branch passage

Fig. 3.5 Feedline geometry for the fuselage analysis

Modal analysis for 60% fuel remaining condition is conducted. The longitudinal modes are extracted based on the modal participation factor, and the first three natural frequencies are compared. In Table 6, results show that the maximum discrepancy in the natural frequencies up to the third mode is 3.2 percent. Also, the transfer functions obtained for both configurations are plotted in Fig. 3.6. The results show that there is a slight increase in the branch passage natural frequencies due to the decreased weight of the feedline components and the fluid inside of them. In fact, compared to the single passage feedline configuration, the structural weight of the branch feedline may be reduced by approximately 35%. This may be advantageous to pogo avoidance because the larger fuselage natural frequencies with branch passage configuration do not coalesce with those of the feedline acoustic modes.

As mentioned in Section 2.3, the location of the feedline inlet becomes different by changing the configuration. Therefore, the eigenvector at the corresponding node location should be considered. Taking this into account, both transfer functions of the fuselage are obtained and compared in Fig. 3.6.

Changes in the natural frequencies due to the feedline geometry is relatively small, but the overall magnitude is affected by the modification of the interface, including the feedline inlet position and the cross-sectional area. The resultant pogo analysis will be conducted based on both transfer functions.

**Table 6 Fuselage mode comparison between the single and branch
passage feedline**

	Single passage	Branch passage	Discrepancy
First mode	12.0Hz	12.1Hz	0.8%
Second mode	18.4Hz	18.8Hz	2.2%
Third mode	28.4Hz	29.3Hz	3.2%

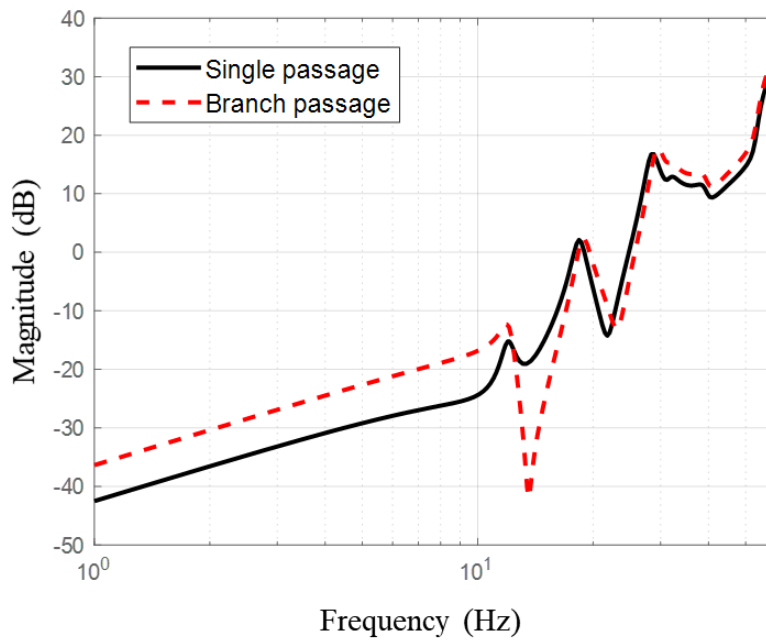


**Fig. 3.6 Transfer function for the fuselage regarding two
feedline configurations**

3.2 Verification of the Feedline Acoustic Mode

To verify the accuracy of the present feedline mode prediction analysis, a flow distribution problem is studied for comparison. In Ref. 28, an experiment was conducted on a T-shaped pipeline flow problem. The geometric properties are provided in Fig. 3.7, and the frequency spectrum of pressure is illustrated in Fig. 3.8. To compare the results, the same configuration is analyzed by the present approach based on the information given. The medium of the fluid in that configuration is water.

From the present analysis, Fig. 3.9 shows the response of the T-shaped feedline frequency results. Comparing the peaks of the transfer function and the frequency spectrum, the differences are shown in Table 7. The table displays the natural frequencies up to 250Hz of the T-shaped system, and a total of 4 modes are sought. While the accuracy is found to degrade as the natural mode frequencies become larger, the method is suitable since a pogo instability is mainly related to the lower mode frequencies at 10 to 60Hz. Thus, this comparison proves that the present analysis will be appropriate for representing the pressure modes of a sophisticated branch pipeline flow distribution.

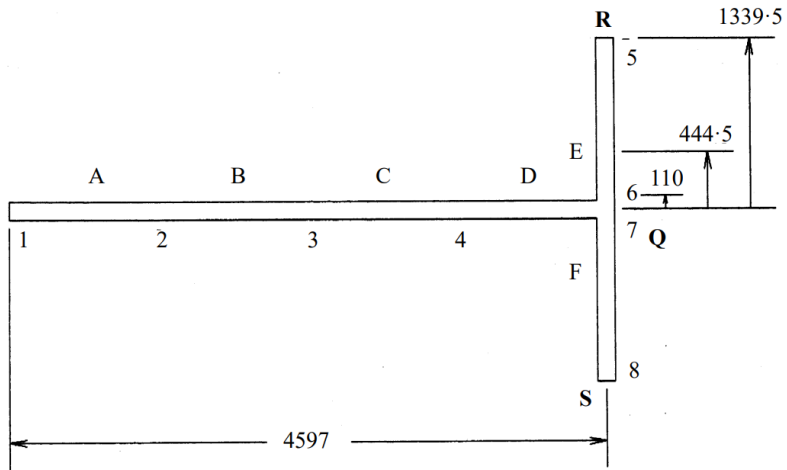


Fig. 3.7 Geometric properties of the experiment [28]

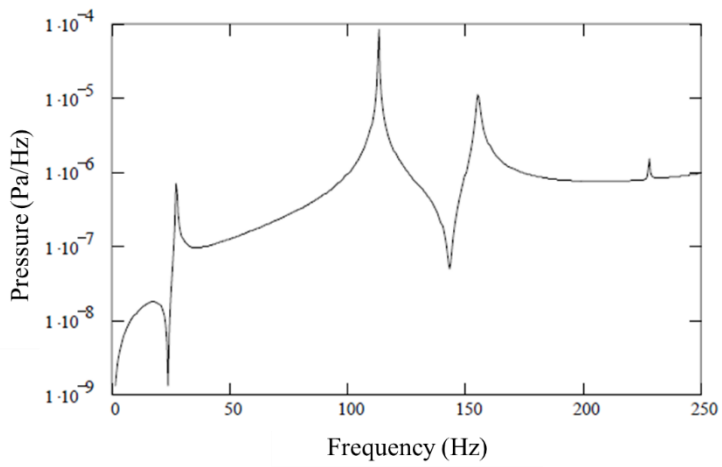


Fig. 3.8 Frequency spectrum of the pressure from the experiment [28]

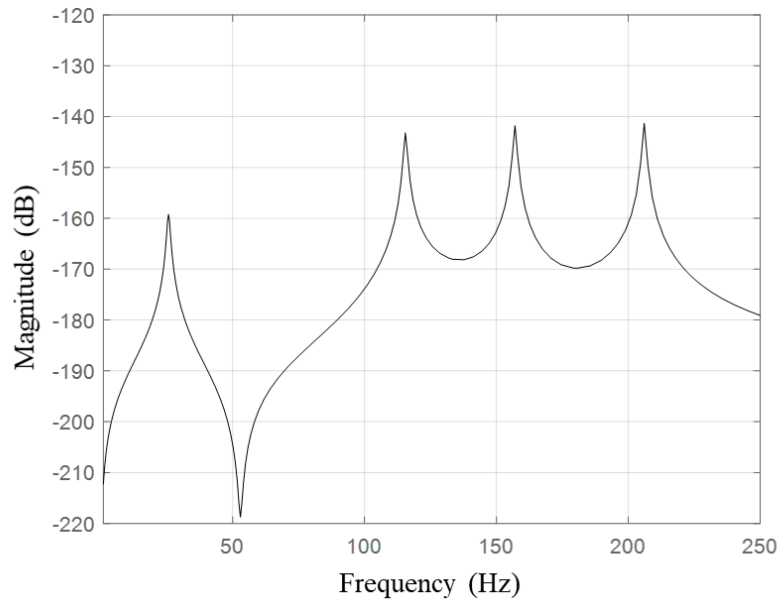


Fig. 3.9 Frequency spectrum result for a T-shaped feedline

Table 7 Feedline mode frequencies against the experimental results

Present (Hz)	Experiment (Hz)	Discrepancy
26	27	3.7%
115	112	2.7%
157	159	1.3%
206	226	8.9%

To predict the pogo resonance, the transfer function of the LOX feedline acoustic mode is to be evaluated. The geometric and the material properties of the present feedline are introduced in Fig. 3.10 and Table 8. System inertance and compliance can be extracted from the fluid characteristics and the geometry. The numerical values can vary depending on the temperature of the liquid within the pipe along with the change of heat capacity mentioned in Fig. 2.3. Thus, Fig. 3.11 shows the compliance per unit length under typical operating condition of the launch vehicle feedline. The maximum of 10.8% discrepancies are found comparing the condition where the feedline is not sufficiently cooled down.

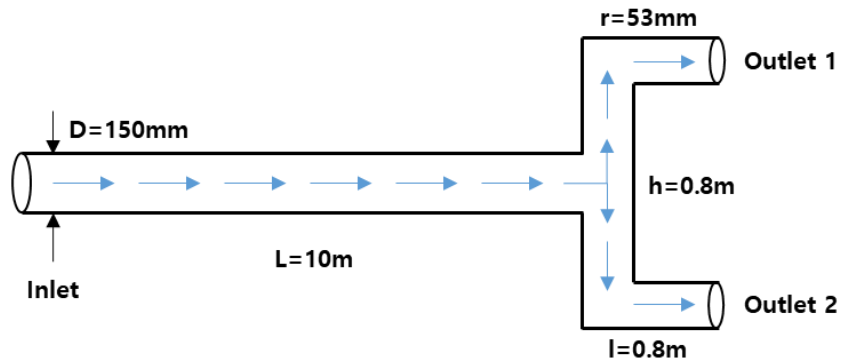


Fig. 3.10 Geometric properties of the present feedline

Table 8 Operating condition and the material properties of the feedline

Property Name	Value	Property Name	Value
Main duct radius (m)	0.075	Outlet mass flow rate (kg/s)	25.0
Main duct length (m)	10.00	Air oxygen speed of sound $c_{AOX}(m/s)$	195.6
Liquid oxygen density $\rho_{LOX}(kg/m^3)$	1126	Air oxygen density $\rho_{AOX}(kg/m^3)$	10.43
Feedline mean temperature(K)	88-108	Feedline mean pressure(MPa)	0.3-2.0

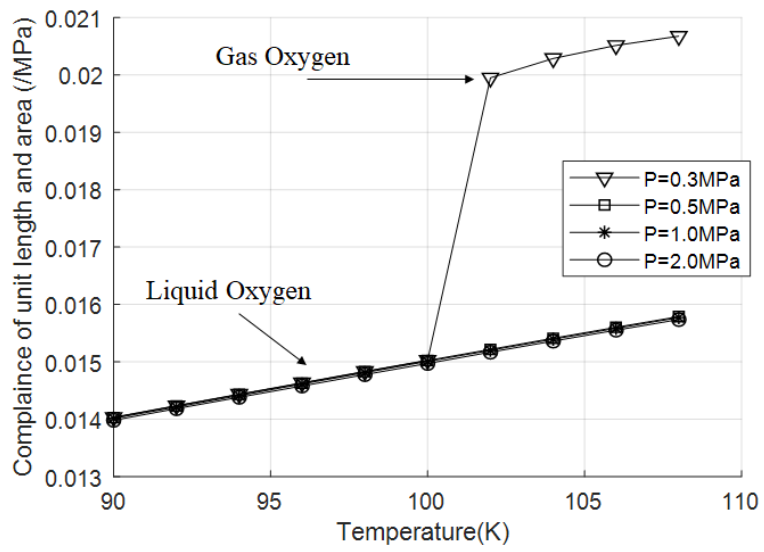


Fig. 3.11 Fluid compliance of unit length and area in terms of temperature

Using the aforementioned configuration, cavitation effect is also included to both ends of the outlets connecting the turbo pump. Figure 3.12 shows the Bode diagram in terms of cavitation volume in the feedline. Depending on the cavitation intensity, natural frequencies and the system response will change. Thus, cavitation volume should be considered for the resonance prediction. It is inferred from the figure that as the cavitation volume increases, the mode frequency of the feedline will decrease. The lowest mode of the system has eigenvalue of 10.1Hz if there exists no cavitation. However, the natural frequency will decrease to 8Hz if cavitation volume of 4% is considered.

Also, since the fluid resistance in Eq. (29) contains a friction factor term, the overall magnitude is affected by the value within the pipeline. Because the friction factor between the fluid and the inner surface of the pipeline is not defined precisely for the launch vehicle, the term is assumed as a variable. In order to see the difference clearly between varying friction factor, Bode plots are drawn for three different conditions in Fig. 3.13. Even with very little change in the value, the magnitudes of the response will be significantly affected. For a few cases, the decrease in the magnitude merges two mode frequencies into a single mode. This will change the total response of the launch vehicle.

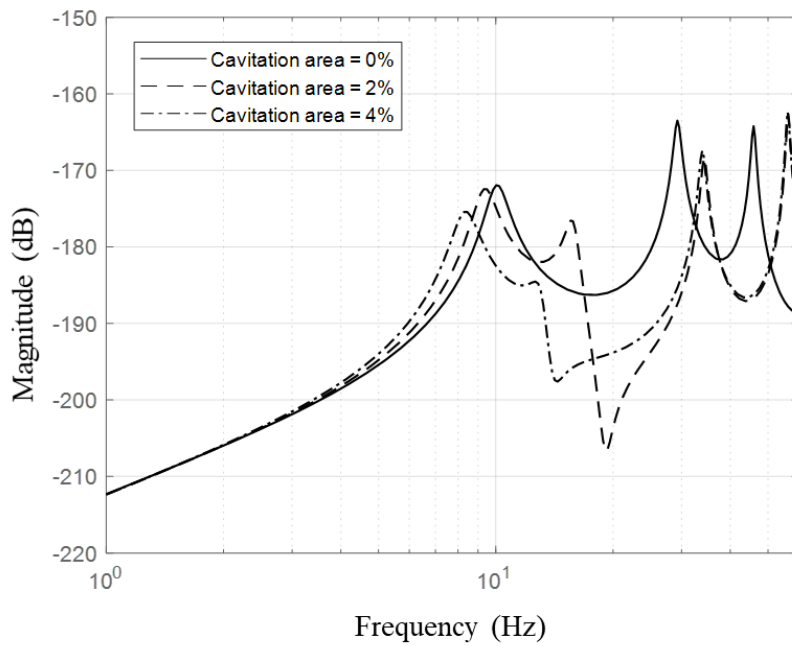


Fig. 3.12 Bode diagram of the feedline modes in terms of the cavitation area(V_{cav}) at the pump inlet (feedline outlet) position

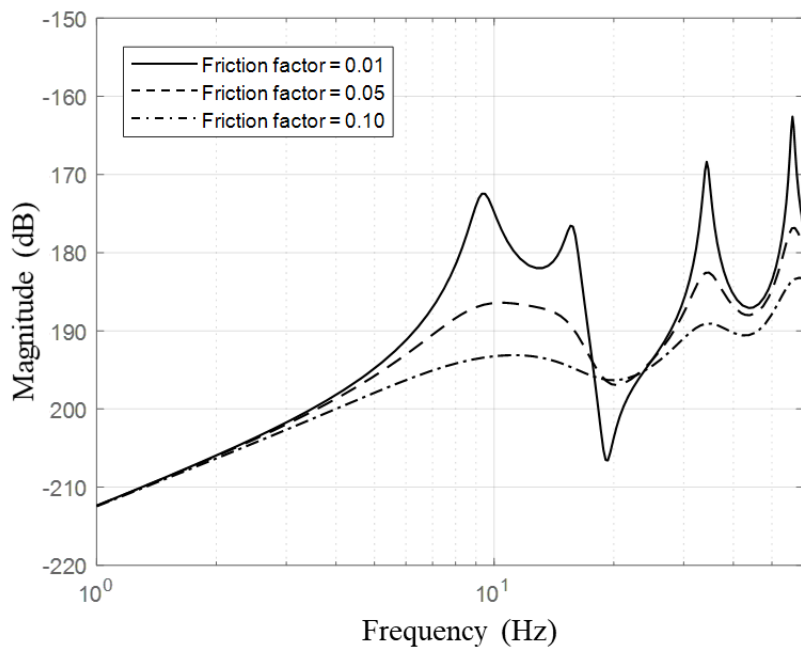


Fig. 3.13 Bode diagram of the feedline in terms of the friction factor

To examine the effect of the flow distribution on the feedline pressure response, transfer functions are compared between the single and branch passage configurations. The sizing dimensions and flow quantities for each are selected in order to provide the same amount of thrust. This signifies that the summation of the mass flow rate illustrated in Fig. 1.1 will be equal between (a) and (b). For clarification, the geometric properties and the operating conditions of the feedline are summarized in Table 9.

Then, the transfer functions of the feedline are compared between the single and branch passage configurations. Bode plots are illustrated in Fig. 3.14. The first mode of the single passage feedline is 12.6Hz, and the corresponding natural frequency is found to be 9.4Hz for the branch pipe passage. The change of dominant natural frequency is mainly due to the change of inertance and the compliance of the fluid networks, which are analogous to M-K terms in a second-order differential equation. Therefore, the pressure modes are obtained by conducting an eigenvalue analysis of the system containing the terms. Also the magnitudes are affected by several factors such as the mass flow rate and the friction factor.

By examining the shift of dominant frequency range of the feedline, comparisons with the fuselage response are carried out.

**Table 9 Geometric properties and operating conditions for the single
and branch passage feedlines**

Property	Single passage	Branch passage
Main feedline length (<i>m</i>)	10	10
Main feedline radius (<i>m</i>)	0.053	0.075
Branch pipe length (<i>m</i>)	-	1.20
Branch pipe radius (<i>m</i>)	-	0.053
Main feedline flow rate (<i>kg/s</i>)	25	50
Average Reynolds number	1.00×10^6	1.41×10^6
LOX speed of sound (<i>m/s</i>)		933
Air oxygen speed of sound (<i>m/s</i>)		196
LOX density (<i>kg/m³</i>)		1126
Air oxygen density (<i>kg/m³</i>)		10.43
Feedline mean temperature (<i>K</i>)		88-108
Feedline mean pressure (<i>MPa</i>)		0.3-2.0

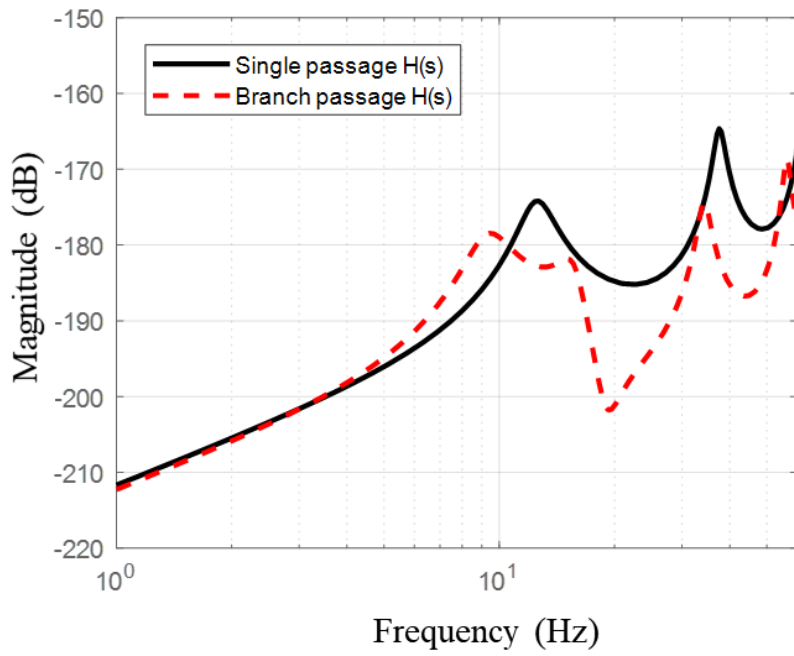


Fig. 3.14 Comparison of the feedline transfer function

Chapter 4

Pogo Instability Analysis

Now that the transfer functions are obtained for both fuselage and feedline modes, the closed loop transfer function synthesis is carried out including the amplification factors of the turbo-pump and the combustor. Numerical analyses for the propulsion components were conducted in the previous studies [29], and the variables are reflected in the formulation. The transfer function of the complete system is obtained by setting the launcher thrust as the input and the inlet node of the LOX feedline as the output. Although the entire process is for a closed loop system, the observation of total response is carried out in series in order to observe the attenuation.

The frequency response functions of the longitudinal dynamics are compared between the single and branch passage configurations to examine the effect of the flow distribution. Figure 4.1 shows the response corresponding to the combination of each fuselage and feedline transfer function. Due to the fact that the natural frequencies of the longitudinal fuselage response lie in the range of 12Hz to 30Hz based on the results of Table 6, the range colored in red should be addressed. From the figure, it is inferred that the overall attenuation is greater for the branch passage configuration. The improved performance is explained in detail through the sine sweep perturbation simulation comparisons.

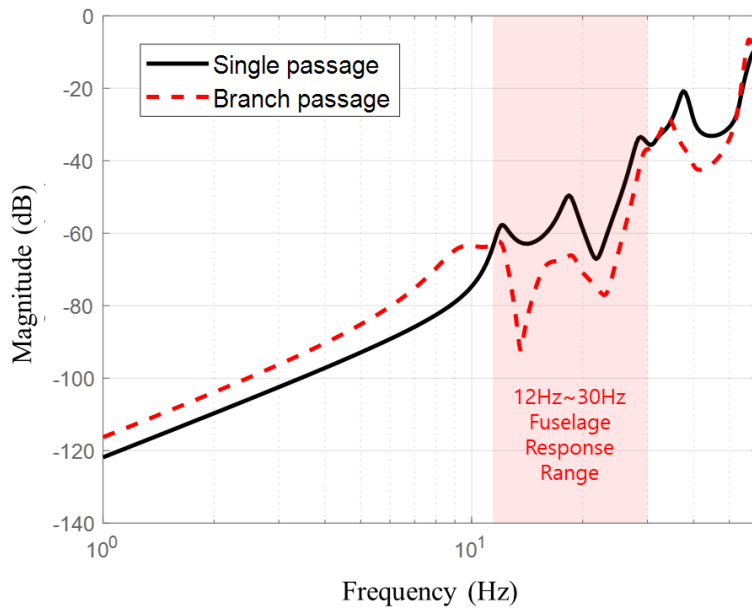
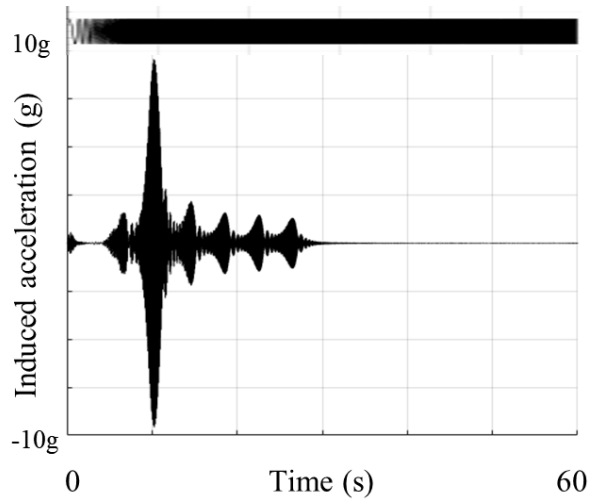


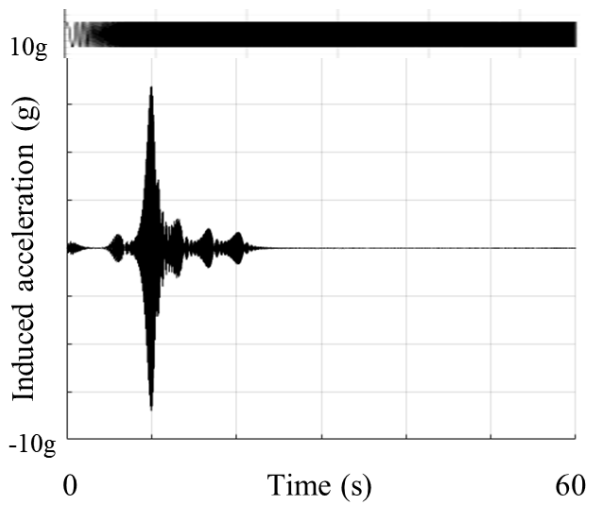
Fig. 4.1 Comparison of the system frequency response function

The transient response of the system is observed by the sine sweep perturbation simulation for system identification as shown in Fig. 4.5. The input perturbation is applied in the form of thrust to the integrated frequency response function shown in Fig. 4.1, and the magnitude of the thrust is determined by considering the total weight of the launch vehicle. The simulation is carried out by sweeping the obtained transfer functions from 0 to 60Hz for a duration of 60 seconds. Through this time-transient sine-sweep analysis, resonant frequencies may be found along with the magnitude. Since the largest response of the fuselage is observed when the remaining fuel level is 60%, two cases are compared under the same fuselage condition.

Figure 4.2 (a) shows the response of the single passage feedline configuration. According to the results shown in the figures, the flow distribution of LOX propellant through the branched feedline suppresses the pressure fluctuation reaching to the inlet of the turbo-pump, leading to a smaller pressure mode and further stable feedback. Although both configurations are exposed to a certain degree of instability, both magnitude and frequency range of the branch passage feedline enforce it to be more robust against the resonance with the fuselage. Compared to a simple straight pipe case, the peak acceleration induced in the transient response is reduced by 5.9%. Also, the attenuation of the resonant modes is improved in Fig. 4.2 (b). Therefore, taking advantage of the branch pipe configuration poses improved stability in terms of the pogo phenomenon.



(a) Single passage feedline



(b) Branch passage feedline

Fig. 4.2 Sine sweep perturbation result of the closed loop response function

Chapter 5

Conclusion and Future Works

5.1 Conclusion

In this thesis, a sophisticated branch-pipe feedline is suggested to analyze the pogo phenomenon that occurs in a clustered liquid rocket engine. Instead of coupling the natural frequencies of the fuselage with the acoustic modes in a single straight LOX pipeline, sophisticated branch-pipe modes are analyzed to account for the various flow distribution situations.

First, fuselage representation with structural damping is constructed and the longitudinal modes are extracted based on the modal participation factor. The modes are realigned and chosen successfully in complicated three-dimensional representation. Convergence examination for the mesh refinement is carried out. MIMO three-dimensional model is then converted into SISO transfer function by specifying the response point at the feedline inlet. With the present transfer function, results are compared with the fuselage modes by the existing lumped parameter methodology. As a result, natural frequencies are found to be similar and the high-fidelity representation shows superior local modal shape prediction. The results show that the pogo-causing frequency range lies between 12 and 30Hz.

Pogo resonance prediction is carried out with fluid transmission line analysis. The system is assumed to have small perturbation so that the nonlinear system may be converted to the linear second-order acoustic response formulation.

Finite element with inertance-resistance-compliance coefficients is used to analyze the flow inside a pipe. Fluid characteristics such as the friction factor, density, heat capacity, and bulk modulus are gathered from the material database. Using such information, system response is analyzed as a SISO form which is capable of extracting damped frequencies and transfer function in terms of the friction factor and cavitation volume.

The two analyses are linked together with a propulsion gain to constitute a complete system. This system is used to calculate the transfer function of thrust to the pump inlet to determine the classical pogo resonance. Using such procedure, response discrepancies are corrected and convergence has been made, and reliable results are obtained for pogo resonance.

According to the present results, the flow distribution of LOX propellant through the branched feedline suppresses the pressure fluctuation reaching to the inlet of the turbo-pump, leading to a smaller pressure mode and further stable feedback. This is mainly due to the fact that the flow distribution rather provides a role like that of an accumulator to increase the compliance and inertance of the fluid networks.

While the response of the simple feedline is exposed to a certain degree of instability, both magnitude and frequency range of the branch-pipe model enforce it to be more robust against the resonance with the fuselage. Compared to a simple straight pipe case, the acceleration induced in the transient response is reduced by 5.9%. Therefore, taking advantage of the branch pipe configuration poses improved stability in terms of the pogo phenomenon.

5.2 Recommendation for Future Works

The present feedline analysis is based on a number of assumptions enlisted in the beginning of Section 2.3, including irrotational and inviscid flow. The method suggested by the previous researchers was based on a one-dimensional finite element representation. The emphasis is made on the flow distribution rather than the precise energy loss due to viscosity and the unusual geometry of the pipeline. Therefore, the following methodology may be required in the future to improve the accuracy of the feedline transfer function analysis. By conducting a series of computational fluid dynamics simulation, the local friction factors will be obtained for various pipeline configurations such as a T-shaped junction or a L-shaped elbow. Since the friction factor is included in the formulation of the resistance, accurate representation of the friction factor will account for the momentum and energy loss within the pipeline where the flow rate and direction changes abruptly.

Also, for further improved pogo stability, pogo accumulator may be installed additionally to the feedline network presented in this thesis. Taking the advantage of the numerical formulation presented herein, the sophisticated fluid networks can be extended to more branching sections for additional engines or accumulators. By doing so, further suppression of the pressure modes in the feedline may be achieved.

Acknowledgments

This work was supported by the Advanced Research Center Program (NRF-2013R1A5A1073861) through a grant from the National Research Foundation of Korea (NRF), which was funded by the Korean government (MSIP) and contracted through the Advanced Space Propulsion Research Center at Seoul National University.

References

- [1] Larsen, C. E., "NASA Experience with Pogo in Human Spaceflight Vehicles," NATO RTO Symposium ATV-152 on Limit-Cycle Oscillations and Other Amplitude-Limited, Self-Excited Vibrations, May, 2008, Norway.
- [2] Wagner, R. G., and Rubin, S., "Detection of Titan Pogo Characteristics by Analysis of Random Data," *Proceedings of ASME Symposium on Stochastic Processes in Dynamical Problems*, Los Angeles, 1969, pp. 51-62.
- [3] Dordain, J. J., Lourme, D., and Estoueig, C., "Study of POGO Effect On Launchers EUROPA-II and DIAMOND," *Acta Astronautica*, Vol. 1, No. 11-12, 1974, pp. 1357-1384.
- [4] Rich, R. L., "Saturn V POGO and a Solution," *AIAA Structural Dynamics and Aeroelasticity Specialist Conference*, New Orleans, 1969.
- [5] Coppolino, R., "A Numerically Efficient Finite Element Hydroelastic Analysis," NASA CR-2662, Apr. 1974.
- [6] Radovich, N. A., "Analytical Model for Missile Axial Oscillation Caused by Engine-Structure Coupling," Lockheed Missiles and Space Company, 1965.
- [7] Worlund, A. L., Hill, R. D., and Murphy, G. L., "Saturn V Longitudinal Oscillation (POGO) Solution," *5th Propulsion Joint Specialist*, AIAA Paper 1969-584, 1969.

- [8] Castenholz, P. J. N. C. "*Investigation of 17-Hz Closed-Loop Instability on S-2 Stage of Saturn 5*," NASA CR-144131, Aug. 1969.
- [9] Lim, B. J., Kim, M. K., Kang, D. H., Kim, H. -J., Kim, J. -G., Choi, H. -S., "Development and Acceptance Test Results of 75-tonf Class Liquid Rocket Engine Gas Generator," *Journal of the Korean Society of Propulsion Engineers*, Vol. 24, No. 4, pp.55-65.
- [10] Rubin, S., "Longitudinal Instability of Liquid Rockets due to Propulsion Feedback/ POGO," *Journal of Spacecraft and Rockets*, Vol. 3, No. 8, 1966, pp. 1188-1195.
- [11] Rubin, S., "*Prevention of Coupled Structure-Propulsion Instability /POGO/ on the Space Shuttle*," NASA SP-8055, Oct. 1970.
- [12] Dotson, K., Rubin, S., and Sako, B., "Effects of Unsteady Pump Cavitation on Propulsion-structure Interaction (POGO) in Liquid Rockets," *45th AIAA/ASME/ASCE/AHS/ASC Structures, Structural Dynamics & Materials Conference*, AIAA Paper 2004-2027, 2004.
- [13] Oppenheim, B. W., and Rubin, S., "Advanced Pogo Stability Analysis for Liquid Rockets," *Journal of Spacecraft and Rockets*, Vol. 30, No. 3, 1993, pp. 360-373.
- [14] Zhao, Z., Ren, G., Yu, Z., Tang, B., and Zhang, Q., "Parameter Study on Pogo Stability of Liquid Rockets," *Journal of Spacecraft and Rockets*, Vol. 48, No. 3, 2011, pp. 537-541.
- [15] Wang, Q., Tan, S., Wu, Z., Yang, Y., and Yu, Z., "Improved Modelling Method of POGO Analysis and Simulation for Liquid Rockets", *Acta*

Astronautica, Vol. 107, Feb.-Mar. 2015, pp. 262-273.

- [16] Chang, H. S., Yeon, J. H., Youn, S. K., Jung, T. K., and Jang, Y. S., "A Study on the Analysis of Pogo Instability and Its Suppression of Liquid Propellant Rocket," *Journal of the Korean Society for Aeronautical & Space Sciences*, Vol. 31, No. 3, 2003, pp. 58-64.
- [17] Sim, J., Kim, J., Lee, S., Shin, S. J., Choi, H., and Yoon, W., "Further Extended Structural Modeling and Modal Analysis of Liquid Propellant Launch Vehicles for Pogo Analysis," *2016 AIAA SPACE and Astronautics Forum and Exposition*, 2016, p. 5648.
- [18] Park, K. J., Lee, S. H., Lee, S. G., and Shin, S. J., "Longitudinal Characteristics Analysis of a Space Launch Vehicle using One and Three-Dimensional Combined Modeling for Pogo Prediction," *2018 AIAA SPACE and Astronautics Forum and Exposition*, 2018, p. 5416.
- [19] Bajura, R. A., and Jones, E. H. Jr., "Flow Distribution Manifolds," *ASME Journal of Fluids Engineering*, Vol. 98, No. 4, 1976, pp. 654–665.
- [20] Reimann, J., and Seeger, W., "Two-Phase flow in a T-junction with a Horizontal Inlet. Part II: Pressure Differences," *International Journal of Multiphase Flow*, Vol. 12, No. 4, Jul.–Aug. 1986, pp. 587-608.
- [21] Xie, F., Xia, S., Chen, E., Li, Y., Mao, H., and Ma, Y., "Numerical Investigation on Instability Flow Behaviors of Liquid Oxygen in a Feeding Pipeline with a Five-Way Spherical Cavity," *Energies*, Vol. 13, No. 4, 2020, pp. 926.

- [22] Kobayashi, K., Oowada, Y., Arita, M., and Nakatsuji, H., "Development Status of H-IIB Launch Vehicle Propulsion System," *Proceedings of the 43rd AIAA/ASME/SAE/ASEE Joint Propulsion Conference & Exhibit*, Cincinnati, Jul. 2007.
- [23] Cho, I. H., Jung, T. K., Jung, Y. S., Kwon, O. S., Oh, S. H., and Lee, D. S., "Development of Korea Sounding Rocket-III Propulsion Feeding System," *39th AIAA/ASME/SAE/ASEE Joint Propulsion Conference and Exhibit*, Alabama, Jul. 2003.
- [24] Michalopoulos, C. D., Clark Jr., R. W., and Doiron, H. H., "Acoustic Modes in Fluid Networks," *The Fourth Annual Thermal and Fluids Analysis Workshop*, NASA, Cleveland, 1992, pp. 169-185.
- [25] Appleby, B., Martin, J. D., and Schuett, R., "*Dynamic Loads Analysis of Space Vehicle Systems-Launch and Exit Phase*", NASA-CR-76502, 1966.
- [26] Lee, S. G., Lee, S. H., Shin, S. J., Kim, Y., and Lee, S., "Pressure Mode Analysis of Nonuniform Cross-sectional Pipes and Preliminary Evaluation of a Pogo Suppressor," *Proceedings of the Institution of Mechanical Engineers, Part G: Journal of Aerospace Engineering*, Vol. 233, No. 12, 2018, pp. 4447-4456.
- [27] Timrot, D. L., and Borisoglebskii, V. P., "The Density of Liquid Oxygen on the Saturation Curve," *Soviet Physics Journal of Experimental and Theoretical Physics*, Vol. 11, No. 6, 1960, pp.1248-1250.

- [28] Vardy, A. E., Fan, D., and Tijsseling, A. S., “Fluid-Structure Interaction in a T-Piece Pipe,” *Journal of Fluids and Structures*, Vol. 10, No. 7, 1996, pp. 763-786.
- [29] Park, K. J., Yoo, J. U., Lee, S. H., Nam, J. H., Kim, H. J., Lee, J. Y., Roh, T. -S., Yoh, J. J., Kim, C. A., and Shin, S. J., “Pogo Accumulator Optimization Based on Multiphysics of Liquid Rockets and Neural Networks,” *AIAA Journal of Spacecraft and Rockets*, Vol. 57, No. 4, July 2020, pp. 809-822.

국문초록

복잡 관망을 포함한 클러스터 액체 추진 로켓의

포고 불안정성 해석

유정욱

서울대학교 대학원

협동과정 우주시스템 전공

우주 발사체에서 동체 구조 및 공급계 사이의 연성(coupling)에 의해 발생할 수 있는 여러 불안정 현상이 존재한다. 그 중, 포고 현상은 발사체 구조의 축 방향 진동으로 인해 공급/추진계 공급라인의 압력 및 유량 모드가 공진하고, 이러한 공진이 동체 구조를 다시 가진 시키는 불안정 현상이다. 이는 주로 포고 억제기를 설치함으로써 비교적 쉽게 해결할 수 있으나, 발사체의 복잡한 동체 모드와 공급관 유량 모드에 대한 정밀한 예측 결과를 얻기 위해서는 실제 형상을 반영한 정교한 모델링이 요구된다.

따라서, 본 연구에서는 액체추진로켓의 포고 불안정성에 대한 수치해석 체계를 구축하고, 이를 이용하여 포고 현상의 발생 여부를 파악하였다. 포고 해석은 구조계, 공급계, 추진계의 주요 모델에 대한 수치해석 결과를 이용하여 수행한다. 구조계는 기존 1 차원 가상 질량-스프링 기법을 3 차원 해석 영역으로 확장하고, 모드

참여 계수 개념을 적용하여 축 방향 동적 전달함수를 확보하였다. LOX 공급계는 탱크의 유체 섭동에 대한 펌프 입구의 응답 해석을 수행하기 위해 fluid transmission line (FTL) 해석을 수행하였다. 특히 클러스터 엔진으로 구성된 발사체의 포고 현상을 해석하기 위해 복잡한 형상의 LOX 공급계를 1 차원 유한요소로 구성하고, 고유치 해석을 수행하여 발사체의 공급/추진계 음향 모드를 추출하였다. 두 갈래로 나뉘지는 분기관 압력 모드 분석하고 전달함수를 추출하여 클러스터형 액체 로켓의 폐루프 제어(closed loop control)를 수행하였다.

그 결과, 분기관 형상의 반영을 통해 공급계의 압력 모드가 동체의 고유진동수로부터 분리되는 경향을 살펴볼 수 있었으며, 공급관의 고유진동수를 변경시킴으로써 동체 구조와의 공진 가능성이 감소하였으며, 포고 억제 능력이 개선되었다.

주요어 : 우주 발사체, 클러스터 엔진, 포고 현상, 포고 억제기,

축 방향 동적 해석, 공급라인 압력 모드

학 번 : 2019-21768